ISTANBUL TECHNICAL UNIVERSITY ★ GRADUATE SCHOOL

CONCEPTUAL POWER CONVERSION ARCHITECTURE FOR UNMANNED AERIAL VEHICLES UTILIZING BLDC MOTOR AS BOTH STARTER AND GENERATOR

M.Sc. THESIS

Emel TİMURKAYNAK SOLAK

Department of Electrical Engineering

Electrical Engineering Programme

JULY 2025

ISTANBUL TECHNICAL UNIVERSITY ★ GRADUATE SCHOOL

CONCEPTUAL POWER CONVERSION ARCHITECTURE FOR UNMANNED AERIAL VEHICLES UTILIZING BLDC MOTOR AS BOTH STARTER AND GENERATOR

M.Sc. THESIS

Emel TİMURKAYNAK SOLAK
(504221011)

Department of Electrical Engineering

Electrical Engineering Programme

Thesis Advisor: Asst. Prof. Dr. Mehmet Onur GÜLBAHÇE

JULY 2025

İSTANBUL TEKNİK ÜNİVERSİTESİ ★ LİSANSÜSTÜ EĞİTİM ENSTİTÜSÜ

BLDC MOTORUN HEM MARŞ MOTORU HEM DE JENERATÖR OLARAK KULLANILDIĞI İNSANSIZ HAVA ARAÇLARI İÇİN KAVRAMSAL GÜÇ DÖNÜŞÜM MİMARİSİ

YÜKSEK LİSANS TEZİ

Emel TİMURKAYNAK SOLAK
(504221011)

Elektrik Mühendisliği Anabilim Dalı

Elektrik Mühendisliği Programı

Tez Danışmanı: Doç. Dr. Mehmet Onur GÜLBAHÇE

TEMMUZ 2025

Emel TİMURKAYNAK SOLAK, a M.Sc. student of İTU Graduate School student ID 504221011, successfully defended the thesis entitled "CONCEPTUAL POWER CONVERSION ARCHITECTURE FOR UNMANNED AERIAL VEHICLES UTILIZING BLDC MOTOR AS BOTH STARTER AND GENERATOR", which she prepared after fulfilling the requirements specified in the associated legislations, before the jury whose signatures are below.

Thesis Advisor :	**Assoc. Prof. Dr. M. Onur GÜLBAHÇE** İstanbul Technical University	.....
Jury Members :	**Assoc. Prof. Dr. D. Ahmet KOCABAŞ** Istanbul Technical University	.....
	Dr. Öğr. Üyesi A. Kubilay ATALAY Istanbul Gedik University	.....

Date of Submission : 29 May 2025
Date of Defense : 02 July 2025

To my spouse,

FOREWORD

First of all, I would like to express my sincere gratitude to my advisor at Istanbul Technical University, Assoc. Prof. Dr. Mehmet Onur GÜLBAHÇE, for the guidance, encouragement and understanding support he has given me throughout this thesis. His patience and enlightening approach have been instrumental in shaping the direction of this study.

I am also deeply grateful to my family for the support and motivation they have given me throughout this process.

Finally, I would like to express my sincere appreciation to my dear husband Ömer SOLAK for his love, support and assistance.

July 2025

Emel TİMURKAYNAK SOLAK
(Electrical Engineer)

TABLE OF CONTENTS

Page

FOREWORD ..... **ix**
TABLE OF CONTENTS ..... **xi**
ABBREVIATIONS ..... **xiii**
SYMBOLS ..... **xv**
LIST OF TABLES ..... **xix**
LIST OF FIGURES ..... **xxi**
SUMMARY ..... **xxiii**
ÖZET…… ..... **xxvii**
1. INTRODUCTION **1**
1.1 Purpose of Thesis 3
1.2 Literature Review 3
2. PROPOSED POWER CONVERSION ARCHITECTURE **11**
2.1 Proposed BLDC Starter-Generator System Design for UAVs 11
2.2 Four Switch Buck Boost Converter 12
2.3 Brushless DC Starter and Generator 14
2.4 Six Step 3 Phase BLDC Inverter/Synchronous Rectifier 17
2.5 Power Loss Comparison of Bidirectional Drives 19
2.6 Proposed System Design Simulations and Discussion 21
3. SYSTEM LEVEL OPTIMIZATION FOR PROPOSED POWER SYSTEM ARCHITECTURE **25**
3.1 Metaheuristic Optimization Methods 25
3.2 Particle Swarm Optimization Algorithm 26
3.3 Proposed System Design and Optimization 29
3.3.1 Loss-Cost-Volume modelling of power stage 29
3.3.2 Loss-Cost-Volume modelling of magnetics 34
3.3.3 Loss-cost-volume modelling of capacitors 36
3.4 Determination of the fitness function 38
3.5 Optimization Results 41
3.5.1 Volume constrainted optimization 41
3.5.2 Cost constrainted optimization 43
3.5.3 Efficiency constrainted optimization 46
4. CONCLUSIONS AND RECOMMENDATIONS **51**
REFERENCES **53**
CURRICULUM VITAE **57**

ABBREVIATIONS

AC : Alternative Current
ACO : Ant Colony Optimization
ADC : Analog to Digital Converter
BLDC : Brushless Direct Current
DC : Direct Current
DCR : Direct Current Resistance
EMF : Electromotive Force
ESR : Equivalent Series Resistance
FA : Firefly Optimization
FSBB : Four Switch Buck Boost
FSBBC : Four Switch Buck Boost Converter
GA : Genetic Algorithm
GaN : Gallium Nitride
HALE : High Altitude Long Endurance
LEV : Light Electric Vehicles
MALE : Medium Altitude Long Endurance
MEA : More Electric Aircraft
HALE : High Altitude Long Endurance
MOSFET : Metal Oxide Semiconductor Field Effect Transistor
PI : Proportional Integral
PM : Permanent Magnet
PMSM : Permanent Magnet Synchronous Machine
PSO : Particle Swarm Algorithm
PWM : Pulse Width Modulation
RMS : Root Mean Square
SA : Simulated Annealing
SiC : Silicon Carbide
UAV : Unmanned Aerial Vehicles

SYMBOLS

C	: Capacitance
H	: The amount of heat
B^y	: Capacitance
C_{cap}	: Cost of the Capacitor
$C_{cap,best}$	: Cost of the Selected (Best) Capacitor
C_{FET}	: Cost of the FET
$C_{FET,best}$	: Cost of the Selected (Best) FET
$C_{heatsink}$	: Cost of the Heatsink
$C_{heatsink,best}$	: Cost of the Selected (Best) Heatsink
C_{ind}	: Cost of the Inductor
$C_{ind,best}$	: Cost of the Selected (Best) Inductor
C_{oss}	: Output Capacitance
D	: Duty Cycle
$f_{opt,cap}$	: Optimal Switching Frequency for the Capacitor
$f_{opt,FET}$	: Optimal Switching Frequency for the FET
$f_{opt,heatsink}$	: Optimal Switching Frequency for the Heatsink
$f_{opt,ind}$	: Optimal Switching Frequency for the Inductor
f_{sw}	: Switching Frequency
I_{avg}	: Average Current
I_{cap}	: Current Through the Capacitor
I_{rms}	: Root Mean Square Current
K_1	: Material Constant
M	: Voltage Gain
P_{ACR}	: Alternating Current Resistance Loss
P_{cap}	: Capacitor Power Loss
$P_{cap,best}$	: Power Loss of the Selected (Best) Capacitor
P_{cond}	: Conduction Power Loss
P_{core}	: Core Loss
P_{coss}	: Output Capacitance Loss
P_d	: Diode Power Loss
P_{DCR}	: Direct Current Resistance Loss

P_{ds} : Drain-to-Source Power Loss

P_{FET} : Power Loss of the FET

$P_{FET,best}$: Power Loss of the Selected (Best) FET

P_{g} : Gate Drive Power Loss

$P_{heatsink}$: Power Loss of the Heatsink

$P_{heatsink,best}$: Power Loss of the Selected (Best) Heatsink

P_{ind} : Power Loss of the Inductor

$P_{ind,best}$: Power Loss of the Selected (Best) Inductor

P_{rr} : Reverse Recovery Power Loss

P_{sw} : Switching Power Loss

P_{total} : Total Power Loss

Q_{g} : Gate Charge

Q_{rr} : Reverse Recovery Charge

R_{DCR} : DC Resistance

$R_{DS(on)}$: Drain-to-Source On Resistance

$R_{ESR,cap}$: Equivalent Series Resistance of the Capacitor

t_{off} : Turn off Time

t_{on} : Turn on Time

V_{cap} : Voltage across the Capacitor

$V_{cap,best}$: Voltage across the Selected (Best) Capacitor

V_{dc} : Direct Current Voltage

V_{ds} : Drain-to-Source Voltage

V_{f} : Forward Voltage of Diode

V_{FET} : Voltage across the FET

$V_{FET,best}$: Voltage across the Selected (Best) FET

V_{gs} : Gate-to-Source Voltage

$V_{heatsink}$: Volume of the Heatsink

$V_{heatsink,best}$: Volume of the Selected (Best) Heatsink

V_{in} : Voltage across the Selected (Best) Inductor

V_{ind} : Voltage across the Inductor

$V_{ind,best}$: Gate-to-Source Voltage of FET

V_{out} : Output Voltage

w : Angular Velocity

α : Weight Coefficient for Volume

β : Weight Coefficient for Cost

γ	**:** Weight Coefficient for Loss
η	**:** Efficiency
Ω	**:** Ohm

LIST OF TABLES

Page

Table 1.1 : Seperate Starter-Generator configuration of UAVs. **6**
Table 1.2 : Integrated Starter-Generator configuration of UAVs. **8**
Table 2.1 : Starter mode parameters. **22**
Table 2.2 : Generator mode parameters. **22**
Table 3.1 : Optimum switch parameters under volume constraints. **41**
Table 3.2 : Optimum capacitor parameters under volume constraints. **41**
Table 3.3 : Optimum inductor parameters under volume constraints. **42**
Table 3.4 : Optimum heatsink parameters under volume constraints. **42**
Table 3.5 : Optimum switch parameters under cost constraints. **44**
Table 3.6 : Optimum capacitor parameters under cost constraints. **44**
Table 3.7 : Optimum inductor parameters under cost constraints. **44**
Table 3.8 : Optimum heatsink parameters under cost constraints. **44**
Table 3.9 : Optimum switch parameters under efficiency constraints. **46**
Table 3.10 : Optimum capacitor parameters under efficiency constraints. **46**
Table 3.11 : Optimum inductor parameters under efficiency constraints. **47**
Table 3.12 : Optimum heatsink parameters under efficiency constraints. **47**
Table 3.13 : All results comparison. **48**

LIST OF FIGURES

Page

Figure 1.1 : Separate Starter-Generator Configuration of UAVs. **5**
Figure 1.2 : Integrated Starter-Generator configuration of UAVs. **7**
Figure 1.3 : BLDC Starter-Generator configuration of UAVs. **9**
Figure 2.1 : Proposed BLDC starter generator system design for UAVs. **11**
Figure 2.2 : Four switch buck boost converter. **13**
Figure 2.3 : Four switch buck boost converter buck mode operation. **13**
Figure 2.4 : Four switch buck boost converter boost mode operation. **14**
Figure 2.5 : 3-Phase BLDC motor structure and parts [39]. **15**
Figure 2.6 : The structure of BLDC [40]. **15**
Figure 2.7 : BLDC motor phase voltages. **16**
Figure 2.8 : Six step drive system for BLDC motor [42]. **18**
Figure 2.9 : Trapezoidal Back EMF. **19**
Figure 2.10 : Starter mode power flow [44]. **19**
Figure 2.11 : Generator mode power flow [44]. **20**
Figure 2.12 : Starter mode simulation model. **22**
Figure 2.13 : Generator mode simulation model. **22**
Figure 2.14 : Starter mode stator current and voltage graph. **23**
Figure 2.15 : Generator mode stator current and voltage graph. **23**
Figure 3.1 : Particle swarm optimization algorithm flowchart. **27**
Figure 3.2 : Proposed algorithm flowchart. **40**
Figure 3.3 : Total losses of the volume constrained design. **42**
Figure 3.4 : Total volume of the volume constrained design. **43**
Figure 3.5 : Total cost of the volume constrained design. **43**
Figure 3.6 : Total losses of the cost constrained design. **45**
Figure 3.7 : Total volume of the cost constrained design. **45**
Figure 3.8 : Total cost of the cost constrained design. **46**
Figure 3.9 : Total losses of the efficiency constrained design. **47**
Figure 3.10 : Total volume of the efficiency constrained design. **48**
Figure 3.11 : Total cost of the efficiency constrained design. **48**

CONCEPTUAL POWER CONVERSION ARCHITECTURE FOR UNMANNED AERIAL VEHICLES UTILIZING BLDC MOTOR AS BOTH STARTER AND GENERATOR

SUMMARY

Today, Unmanned Aerial Vehicles (UAVs) play a critical role in a wide range of fields, including defense, logistics, agriculture, surveillance, and industrial automation. The operational performance of these systems is directly dependent on factors such as high efficiency, extended flight range, and low overall weight. However, traditional power system architectures commonly employ separate starter motors and generators, which increase the total system weight, add wiring complexity, and lead to inefficiencies in energy management. These conventional configurations also present technical limitations, such as integration difficulties and limited energy recovery capabilities.

To address these challenges, this study proposes an integrated power system architecture based on a Brushless Direct Current (BLDC) motor. In the proposed configuration, the BLDC motor functions as both a starter and a generator, effectively reducing overall system weight and component complexity. The system combines a Four Switch Buck Boost Converter (FSBBC) and a Three Phase Inverter to enable bidirectional energy transfer and dynamic power management across various UAV flight phases.

The FSBBC operates in either step-up (boost) or step-down (buck) mode depending on system requirements. During the starting phase, it supplies sufficient voltage to the BLDC motor, while in generator mode, it regulates the generated energy to match the system voltage. Compared to conventional converter topologies, the four switch configuration reduces switching losses and the number of components, thereby enhancing overall system efficiency and reliability.

The Three Phase Inverter is another critical component, responsible for both driving the BLDC motor and rectifying the energy produced in generator mode. During startup, the inverter converts Direct Current (DC) power into three phase Alternative Current (AC) to drive the motor; in generator mode, it performs the inverse function by converting the generated AC power back into DC. Controlled by Pulse Width Modulation (PWM), the inverter enables precise torque and speed control of the motor.

To ensure stable and efficient operation during mode transitions, a Proportional-Integral (PI) control strategy is implemented. This control algorithm dynamically adjusts switching signals for the converter and inverter, allowing the system to maintain stable voltage and current levels under varying flight conditions. The PI controller also helps prevent voltage irregularities during mode changes, thereby maintaining energy continuity and system safety.

The proposed integrated power system architecture was evaluated through detailed simulations conducted in MATLAB/Simulink. The results confirmed the real time control performance, energy efficiency, and suitability of the system for UAV

applications. Simulations demonstrated that the BLDC-based integrated starter generator system can operate reliably in both modes, delivering high conversion efficiency and uninterrupted bidirectional power flow. The PI controller effectively stabilized voltage and current during transitions, minimizing sudden disturbances and energy losses.

The system was observed to achieve approximately 15–20% higher energy recovery compared to traditional unidirectional power converters. This improvement is attributed to the FSBBC's bidirectional operation, which enables efficient energy feedback to the power system during various flight phases. Enhanced energy recovery is especially beneficial for long-endurance missions, improving overall energy autonomy.

A key advantage of the proposed system is the reduction in total weight. By integrating the starter and generator functions into a single BLDC motor, the need for two separate electromechanical units is eliminated. This architectural simplification is expected to yield up to a 30% reduction in weight, based on future hardware implementations. Reduced weight translates directly into increased payload capacity, improved maneuverability, and enhanced overall system performance for UAVs.

In future work, the proposed system will be experimentally validated. Through hardware implementation, the impact of real-world environmental factorssuch as temperature variations, vibrations, and electromagnetic interferenceon system performance will be assessed. Additionally, emerging semiconductor technologies in power electronics, such as Gallium Nitride (GaN) and Silicon Carbide (SiC) MetalOxide Semiconductor Field Effect Transistors(MOSFET), offer the potential to further improve power conversion efficiency, power density, and thermal performance. These materials exhibit superior electrical and thermal characteristics compared to traditional silicon-based MOSFETs, making them highly suitable for high-performance UAV power systems.

In this study, not only was the system architecture developed, but a multicriteria optimization approach was also applied to maximize the system's performance in terms of energy efficiency, volume, and cost parameters. The selection of the hardware components of the developed BLDCbased integrated starter generator system including power semiconductors, inductor, capacitor, and heatsink was optimized by considering the system's total power loss, total volume, and unit cost. In this context, a Particle Swarm Optimization (PSO) algorithm was employed to perform a parametric search over each component's database, allowing the evaluation of numerous design variables that affect overall system performance.

The objective function used in the optimization process is defined to take into account three basic criteria. The first of these is the total power loss in the system (including conduction, switching, core, equivalent series resistance and gate losses), the second is the total volume of the system (including semiconductor power elements, magnetic elements and coolers) and finally the total cost (based on unit prices). This multi-objective function was transformed into a single objective function by the weighted combination method and the most optimal structure suitable for the system's mission conditions was determined by evaluating different weight scenarios. Simulation and optimization outputs showed that the proposed system operates with high performance not only with its integrated structure but also thanks to the precision determination of the selected components.

As a result, the BLDC enginebased integrated power system architecture proposed in this study offers significant advantages in terms of both energy conversion efficiency and structural improvement, and stands out as an important alternative in the field of energy management in new generation UAV designs. In addition, this holistic approach based on optimization ensured that the integrated power system architecture operates in ideal conditions not only structurally and functionally, but also numerically. In this way, the system stands out as a highly efficient and compact solution that can adapt to variable power demands in different flight phases. The optimization approach is considered as a powerful tool that will facilitate the scaling of the proposed architecture to different UAV platforms, larger power levels and hybrid electric systems in the future.

BLDC MOTORUN HEM MARŞ MOTORU HEM DE JENERATÖR OLARAK KULLANILDIĞI İNSANSIZ HAVA ARAÇLARI İÇİN KAVRAMSAL GÜÇ DÖNÜŞÜM MİMARİSİ

ÖZET

Günümüzde İnsansız Hava Araçları (İHA), savunma, lojistik, tarım, gözetim ve endüstriyel otomasyon gibi birçok alanda kritik bir rol oynamaktadır. Bu sistemlerin operasyonel başarımı, yüksek verimlilik, uzun menzil ve düşük ağırlık gibi performans kriterlerine doğrudan bağlıdır. Ancak mevcut güç sistemlerinde yaygın olarak kullanılan ayrı marş motoru ve generatör yapıları, sistemin toplam ağırlığını ve kablolama karmaşıklığını artırmakta ve enerji yönetiminde verimlilik kayıplarına yol açmaktadır. Bu geleneksel mimariler, entegrasyon zorlukları ve sınırlı enerji geri kazanım oranları gibi çeşitli teknik kısıtlamaları da beraberinde getirmektedir.

Bu çalışma, söz konusu sınırlamaları aşmak amacıyla, Fırçasız Doğru Akım (FDA) motor tabanlı entegre bir güç sistemi mimarisi önermektedir. Geliştirilen yapı, FDA motorun hem marş motoru hem de generatör olarak çalışmasına olanak tanımakta ve böylece sistemin hem ağırlığını hem de bileşen karmaşıklığını azaltmaktadır. Bu çift işlevli sistemde, Dört Anahtarlı Düşürücü-Yükseltici Dönüştürücü (DADYD) ile Üç Fazlı Evirici bir araya getirilerek, çift yönlü enerji dönüşümü gerçekleştirilmekte ve farklı uçuş fazlarında dinamik enerji yönetimi sağlanmaktadır.

DADYD, sistemin ihtiyaçlarına göreyükseltici veya düşürücümodlarında çalışarak, başlangıç fazında motora uygun gerilimi sağlar, generatör modunda ise üretilen enerjiyi düzenleyerek sistem gerilimine uyumlu hale getirir. Dört anahtarlı topoloji, klasik dönüştürücülere kıyasla daha düşük anahtarlama kayıpları ve daha az bileşen gereksinimi sunarak sistemin toplam verimliliğini ve güvenilirliğini artırmaktadır.

Üç Fazlı Evirici ise, FDA motorun sürülmesini ve generatör modunda üretilen enerjinin doğrultulmasını sağlayan temel bileşendir. Başlatma aşamasında Doğru Akım (DA) kaynağından aldığı enerjiyi üç fazlı Alternatif Akıma (AA) dönüştürerek motoru tahrik ederken, generatör moduna geçildiğinde ise üretilen AA enerjiyi DA'ya çevirerek tekrar güç sistemine kazandırır. Darbe Genişlik Modülasyonu (DGM) tekniğiyle kontrol edilen evirici, motorun tork ve hız kontrolünü yüksek hassasiyetle gerçekleştirmektedir.

Sistemdeki tüm geçişlerin kararlı ve verimli biçimde yönetilebilmesi için Oransal-İntegratör (Oİ) kontrol stratejisi uygulanmıştır. Bu denetim algoritması, dönüştürücü ve evirici üzerindeki kontrol sinyallerini dinamik olarak ayarlayarak, sistemin çeşitli uçuş koşullarında kararlı gerilim ve akım değerlerinde çalışmasını sağlar. Bu sayede mod geçişlerinde oluşabilecek gerilim düzensizliklerini önleyerek hem enerji sürekliliğini hem de sistem güvenliğini garanti altına alır.

Önerilen entegre güç sistemi mimarisi, MATLAB/Simulink ortamında gerçekleştirilen ayrıntılı benzetim çalışmalarıyla değerlendirilmiş; sistemin gerçek zamanlı kontrol başarımı, enerji verimliliği ve İHA uygulamaları için uygunluğu ortaya konulmuştur.

Gerçekleştirilen benzetim çalışmaları, önerilen FDA motor tabanlı entegre starter generatör sisteminin hem marş hem de generatör modlarında kararlı ve yüksek verimle çalışabildiğini göstermiştir. Sistem, DADYD ve Üç Fazlı Evirici'nin entegre edilmesiyle çift yönlü enerji akışını kesintisiz şekilde gerçekleştirebilmektedir. Böylece enerji dönüşüm verimliliğini ve sistem istikrarını önemli ölçüde artırmaktadır. Uygulanan Oİ kontrol stratejisi sayesinde, mod geçişleri sırasında gerilim ve akım seviyeleri sabit tutulmakta, ani dalgalanmaların ve enerji kayıplarının önüne geçilmektedir.

Önerilen sistemin geleneksel tek yönlü dönüştürücülere kıyasla yaklaşık %15 ila %20 oranında daha yüksek enerji geri kazanım oranı sunduğu gözlemlenmiştir. Bu iyileşme, DADYD'nin çift yönlü çalışma kabiliyeti sayesinde, uçuşun farklı evrelerinde üretilen enerjinin etkili bir şekilde güç kaynağına geri aktarılabilmesi sayesinde gerçekleşmektedir. Enerji geri kazanımındaki bu artış, uzun menzilli görevlerde enerji otonomisi açısından kritik bir avantaj sağlamaktadır.

Sistemin en önemli katkılarından biri de toplam ağırlığın azaltılmasıdır. Marş motoru ve generatör işlevlerinin tek bir FDA motorunda birleştirilmesi sayesinde, geleneksel yapılarda yer alan iki ayrı elektromekanik birime olan ihtiyaç ortadan kaldırılmıştır. Bu entegrasyonun, donanım düzeyinde yapılacak uygulamalarla %30'a varan bir ağırlık azalması sağlaması beklenmektedir. Ağırlığın azaltılması, İHA'nın taşıma kapasitesini artırmakta, manevra kabiliyetini geliştirmekte ve genel operasyonel verimliliği desteklemektedir.

Gelecekteki çalışmalar kapsamında, önerilen sistemin deneysel olarak doğrulanması hedeflenmektedir. Donanım düzeyinde gerçekleştirilecek uygulamalarla, çevresel faktörlerin (örneğin sıcaklık değişimleri, titreşimler, elektromanyetik parazitler) sistem performansı üzerindeki etkileri değerlendirilebilecek; böylece sistemin pratikteki uygulanabilirliği ortaya konulabilecektir. Ayrıca güç elektroniği alanında gelişmekte olan yarı iletken teknolojileri (örneğin, Galyum Nitritve Silisyum Karbür), daha düşük anahtarlama kayıpları, yüksek güç yoğunluğu ve termal performans gibi avantajlarıyla sistem verimliliğini daha da artırma potansiyeline sahiptir. Bu malzemeler, geleneksel silikon tabanlı yarı iletkenlere kıyasla üstün elektriksel ve termal özellikler sundukları için, yüksek performanslı İHA güç sistemlerinde ideal bir çözüm olarak değerlendirilmektedir.

Bu çalışmada yalnızca sistem mimarisi geliştirilmekle kalınmamış, aynı zamanda sistemin enerji verimliliği, hacim ve maliyet parametreleri açısından performansının en üst düzeye çıkarılması amacıyla çok kriterli optimizasyon yaklaşımı da uygulanmıştır. Geliştirilen FDA tabanlı entegre starter generatör sisteminin donanımsal bileşenlerinin (yarı iletken güç elemanları, endüktör, kapasitör ve soğutucu) seçimi, sistemin toplam güç kaybı, hacmi ve birim maliyeti göz önünde bulundurularak optimize edilmiştir. Bu kapsamda, Parçacık Sürü Optimizasyonu (PSO) algoritması kullanılarak, her bir bileşenin veritabanı üzerinden parametrik taraması gerçekleştirilmiş ve sistemin toplam performansını etkileyen çok sayıda tasarım değişkeni denetlenmiştir.

Optimizasyon sürecinde kullanılan amaç fonksiyonu, üç temel kriteri dikkate alacak şekilde tanımlanmıştır. Bunlardan ilki sistemdeki toplam güç kaybı (iletim, anahtarlama, çekirdek, eşdeğer seri direnç ve kapı kayıpları dahil), ikincisi sistemin toplam hacmi (yarı iletken güç elemanları, manyetik elemanlar ve soğutucular dahil) ve son olarak toplam maliyetidir (birim fiyatlara dayalı). Bu çok amaçlı fonksiyon, ağırlıklı birleştirme yöntemiyle tekil bir hedef fonksiyon hâline getirilmiş ve farklı

ağırlık senaryoları değerlendirilerek sistemin görev koşullarına uygun en optimal yapı belirlenmiştir. Simülasyon ve optimizasyon çıktıları, önerilen sistemin yalnızca entegre yapısıyla değil, aynı zamanda seçilen bileşenlerin hassasiyetle belirlenmesi sayesinde de yüksek performanslı çalıştığını göstermiştir.

Sonuç olarak, bu çalışma ile önerilen FDA motor tabanlı entegre güç sistemi mimarisi, hem enerji dönüşüm verimliliği hem de yapısal iyileştirme açısından önemli avantajlar sunmakta olup, yeni nesil İHA tasarımlarında enerji yönetimi alanında önemli bir alternatif olarak öne çıkmaktadır. Bununla birlikte de optimizasyon tabanlı bu bütünsel yaklaşım, entegre güç sistemi mimarisinin sadece yapısal ve işlevsel değil, aynı zamanda sayısal olarak da ideal koşullarda çalışmasını sağlamıştır. Bu sayede sistem, farklı uçuş fazlarında değişken güç taleplerine uyum sağlayabilen, yüksek verimli ve kompakt bir çözüm olarak öne çıkmaktadır. Optimizasyon yaklaşımı, önerilen mimarinin gelecekte farklı İHA platformlarına, daha büyük güç seviyelerine ve hibrit elektrikli sistemlere ölçeklenmesini kolaylaştıracak güçlü bir araç olarak değerlendirilmektedir.

1. INTRODUCTION

UAVs are widely used in a wide range of applications, especially in the defense industry, agriculture, disaster management, cargo transportation, environmental surveillance and border security. These platforms must simultaneously provide features such as lightness, long flight duration, energy efficiency and ease of system integration in order to increase their operational efficiency. In this context, the energy production and management infrastructure of UAV systems plays a direct determining role in the overall performance of the carrier platform. Today, starter and generator systems are designed separately in many aircraft; this leads to various disadvantages such as increased weight, complex cabling system, low energy recovery rates and maintenance difficulties. In order to overcome these problems, integrated system solutions that combine starter and generator functions on a single electric machine have come to the fore in both defense and civil aviation in recent years. These approaches both simplify the system architecture and have the potential to increase total energy efficiency by providing regenerative energy recovery during the flight. Most of the existing integrated starter generator systems consist of direct current motors, polyphase PMSM motors and BLDC motors [1-3]. These systems also bring disadvantages such as complex control algorithms, high processor load, increased switching losses and system cost.

In this thesis, the system proposed as an alternative to the above disadvantages is a compact and low loss power system architecture in which a BLDC motor driven by a 6 step commutation method assumes both the starter and generator functions, and this motor is directly connected to the DC bus via a FSBB converter. In this system, the motor performs the starter function by receiving energy during take off while the FSBB converter is in boost mode, while during flight it converts mechanical energy into electrical energy and feeds the bus in the FSBB converter buck mode, thus assuming the generator function. Thus, by providing bidirectional energy flow, the same structure is used for both take off and energy recovery, the total number of system

components is reduced and efficiency is increased. The originality of the system can be gathered under three mainheadings:

• The preference of 6 step commutation provides applicability with much simpler control algorithms compared to traditional sinusoidal controls, reduces the load on the processor and offers a delay free motor drive.

• The use of a FSBB converter requires fewer switching elements than a six switch classical inverter structure, reducing both hardware complexity and switching losses. In addition, this structure can operate in systems with fixed DC bus voltage.
• The integration of starter and generator functions in a single BLDC machine reduces system weight by up to 30% and facilitates system integration.

The architecture described above is particularly suitable for small and medium-sized UAVs where weight and volume limitations are critical. In addition, indirect contributions such as increasing the energy recovery rate, extending the battery life and reducing the thermal load are also positively reflected in the system performance. In this study, it is aimed to model the designed system in MATLAB/Simulink environment, perform power flow analyses in start up and generator modes, calculate switching, transmission and regenerative losses and evaluate the preferred motor converter structure in comparison with traditional solutions.

In addition, PSO, one of the metaheuristic methods, will be used to determine the parameters that will ensure the maximum efficiency of the system, and multiple targets such as system volume, weight and cost will be taken into account while minimizing the losses.

In this context, this thesis study presents the detailed modeling, analysis and optimization of an architecture that operates with less losses, contains fewer elements and is simpler in terms of control, unlike the integrated starter generator systems common in the literature. The proposed approach is an important step towards providing more efficient, lightweight and flexible power systems for next-generation UAV systems.

1.1 Purpose of Thesis

The aim of this thesis is to design and analyze a compact, highly efficient and optimized power system driven by a FSBB converter, which performs both starter and generator functions via a single BLDC motor, to be used in UAVs. The system is driven by a simple 6 step commutation method; Thanks to the FSBB structure, bidirectional energy flow between the motor and the DC bus is provided, enabling both start up and regenerative energy recovery. During the design process, the semiconductor switching elements used were selected according to their thermal and electrical properties; the transmission, switching and drive losses of the system were analyzed in detail. In addition, the appropriate heat sink was selected in line with the cooling requirements; finally, it was aimed to simultaneously minimize the total system losses, volume and cost with the PSO method. Thus, a low cost and highly efficient integrated starter generator architecture applicable under real UAV conditions was presented.

1.2 Literature Review

The development of BLDC starter generator systems has become increasingly important in the context of modern aviation engineering, particularly within More Electric Aircraft (MEA) architectures. These integrated systems significantly increase the efficiency, reliability and sustainability of aircraft electrical systems by simultaneously performing engine start and power generation functions [4, 5].

One of the main advantages of BLDC based starter generators is their compact structure and lightweight design. These features are critical in aerospace applications where improving fuel economy and increasing payload capacity are of paramount importance [5]. Additionally, meeting the demanding requirements of power quality, efficiency, and reliability in aeronautical electrical systems necessitates the development of advanced starter generator topologies [6].

In terms of functionality, BLDC starter generators typically use a wound rotor synchronous machine architecture. This design provides an advantage in high reliability aviation applications by allowing seamless transitions between starter and generator modes [7]. Furthermore, the elimination of brushes reduces maintenance

requirements, eliminates the possibility of failure, and increases overall system reliability [4, 8].

Control strategies also play an important role in optimizing the performance of BLDC starter generators. Rotor position estimation techniques are essential to ensure efficient transitions between starting and generating modes [9]. In addition, active excitation control methods developed for three stage wound rotor systems help increase starting torque and power generation stability while addressing the limitations of traditional configurations [10].

As a result, the integration of BLDC technology into starter generator modules represents a significant improvement for power systems in the aviation industry. Due to their reduced weight, improved efficiency, and lower maintenance costs, these systems are becoming essential components of MEA and all electric aircraft architectures. Demand for MEA continues to increase, for this reason research and development in BLDC starter generator technologies will play a crucial role in meeting the changing electrical needs of future aircraft.

FSBB converters have recently emerged as an important topology in applications with small size and weight constraints, such as light electric vehicles (LEVs). This converter topology offers stable operation over a wide input voltage range due to its ability to operate in both step down and step-up modes and to enable bidirectional power transfer [11, 12]. As in LEVs, UAVs typically rely on a single DC bus to power various subsystems. Therefore, FSBB converters are considered quite suitable for UAV electrical architectures, especially in scenarios requiring variable voltage levels, lightweight design and high efficiency. However, among the disadvantages of this topology, the conduction losses in the high side switches due to their continuous operation stand out. Choosing the appropriate semiconductor devices allows to optimize the converter performance and eliminates this disadvantage.

When examining the electrical power systems in unmanned aerial vehicles, it is seen that there are different types of power architectures. Whether the starter and generator are integrated or separate in UAVs often depends on factors such as the type of engine used in the UAV, power requirements, and operational concept. When internal combustion piston engines are used in UAVs, the starter motor and generator are usually designed as separate units in order to provide the engine's initial start and

generating electricity during operation. This approach allows different performance needs such as engine starting torque and continuous energy production to be optimized independently [13]. Thus, system efficiency is increased and maintenance processes are simplified.

In UAVs, the design of the electrical power system plays a critical role in efficient energy management and mission success. In particular, pistonengine UAVs use separate starter and generator units to independently manage engine starting and electrical power generation needs. Although this approach is disadvantageous in terms of additional weight and volume compared to integrated starter generator solutions, it provides operational reliability, system modularity and ease of maintenance. A representative structure of the UAVs with separate starter generator configuration is given in Figure 1.1.

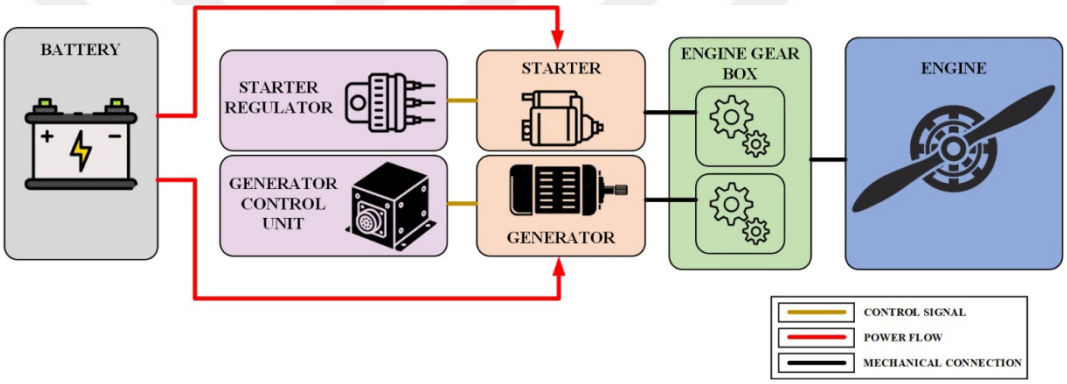

Figure 1.1 : Separate Starter-Generator Configuration of UAVs.

UAVs that use piston engines to meet their propulsion requirements are given in Table 1.1, including the General Atomics MQ-1 Predator, Bayraktar TB2, IAI Heron, Northrop Grumman RQ-5 Hunter, and Anka. In these platforms, the starter and generator systems are located as separate units, which increases operational reliability. It also reflects a design approach that prioritizes independent optimization of engine start and power generation functions. All of these UAVs fall into the Medium Altitude Long Endurance (MALE) category [14-22]. The use of separate starter and generator units provides robustness, but has a weight and volume disadvantage compared to integrated starter generator systems. However, it supports ease of maintenance and fault isolation, which are critical for tactical and strategic operations where mission success and system service life are crucial.

Table 1.1 : Seperate Starter-Generator configuration of UAVs.

UAV Name	Engine Type	Starter-Generator Configuration	Country	Category
General Atomics MQ-1 Predator	Piston Engine (Rotax 914F)	Starter and Generator Separate	USA	MALE (Medium Altitude Long Endurance)
Bayraktar TB2	Piston Engine (Rotax 912)	Starter and Generator Separate	Türkiye	MALE
IAI Heron	Piston Engine (Rotax 914)	Starter and Generator Separate	Israel	MALE
Northrop Grumman RQ-5 Hunter	Piston Engine (Heavy Fuel Engine - Moto Guzzi)	Starter and Generator Separate	USA	Tactical UAV
Anka	Piston Engine (Thielert Centurion 2.0S - Diesel)	Starter and Generator Separate	Türkiye	MALE

In contrast, in turbine powered UAVs, the starter and generator functions mostly consist of an integrated starter generator system. Considering the high speed requirements, volume and weight saving requirements, these integrated systems provide both high torque at take off and provide advantages in weight and space usage by switching to energy production mode after the engine has gained speed. This integration is also considered one of the cornerstones of the MEA concept [23].

The use of starter generator systems provides significant advantages such as reducing weight, optimizing volume, and increasing power density [13, 23]. A well designed starter generator system offers high efficiency in both modes and improves the overall energy management performance of the system [23]. However, in the event of a failure of a single integrated unit, there is a risk of losing both engine starting and power generation capabilities; therefore, backup power supplies are also integrated into the system on some platforms [24].

Developing UAV technologies include significant innovations not only in aerodynamic design and mission software, but also in power transmission systems. In particular, the architecture of the starter and generator systems has a direct impact on the operational efficiency, reliability and mission success of the platform. In modern UAVs, the engine type and starter generator configuration determine many critical parameters such as system weight, volume, ease of maintenance and fault management. In this context, how starter and generator systems are positioned among

UAV platforms with different mission profiles and engine structures provides an important area of comparison. A representative structure of the UAVs with integrated starter generator configuration is given in Figure 1.2.

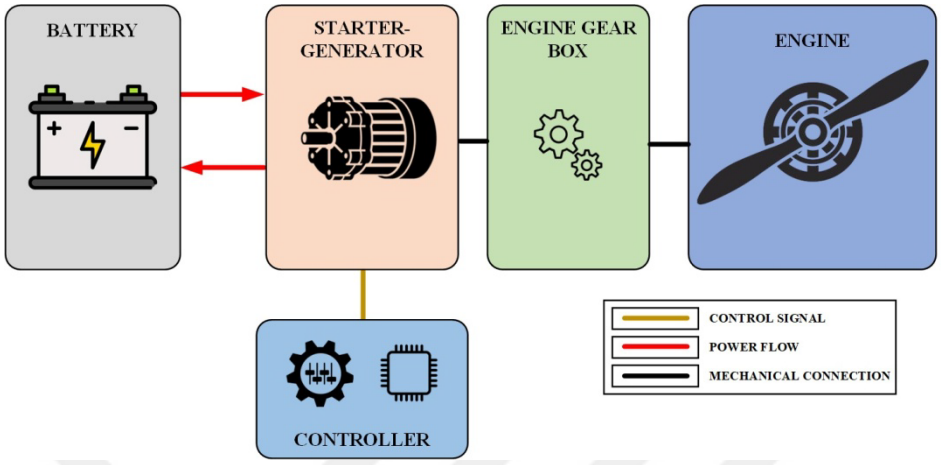

Figure 1.2 : Integrated Starter-Generator configuration of UAVs.

Among the advanced UAVs, Bayraktar Akıncı, MQ-9 Reaper, General Atomics Mojave, Eurodrone (MALE RPAS) and BAE Systems Mantis have different engine and starter generator configurations. The platforms listed in Table 1.2 have been developed for high altitude and long range missions and use turboprop engines and are also equipped with integrated starter generator systems. These integrated structures are preferred to meet the high speed needs of turbine engines and to optimize the volume and weight in the system. The main advantages of integrated starter generator systems are compact volume, high power to weight ratio, increased electrical efficiency and system simplification. Especially in high altitude and long-term missions, weight reduction directly increases the range and endurance capability of the platform. However, integrated structures also have some disadvantages. Combining the starter and generator functions in a single unit increases the risk of the entire system becoming inoperable in the event of a possible failure. In addition, heat management becomes more critical due to high frequency motor operations and power electronic components. Therefore, thermal design and reliability management are of great importance. Bayraktar Akıncı UAV uses twin turboprop engines (PT6A-135A or AI-450T) and the starter and generator systems are designed in an integrated structure. This structure provides system compactness, maintenance time and volume advantages. However, having the starter and generator separate increases the overall system volume, limiting potential weight savings. Similarly, European-based

platforms such as Eurodrone (MALE RPAS) and BAE Systems Mantis also prefer integrated starter and generator systems [25-30].

These platforms are classified in the high altitude long endurance (HALE) or MALE categories according to their mission profiles. In general, the engine type and starter generator architecture stand out as a determining design parameter according to the operational requirements of the UAV, weight volume optimization targets and mission profile.

Table 1.2 : Integrated Starter-Generator configuration of UAVs.

UAV Name	Engine Type	Starter-Generator Configuration	Country	Category
Bayraktar Akıncı	Twin Turboprop (AI-450T)	Integrated Starter and Generator	Turkey	HALE
MQ-9 Reaper	Single Turboprop (Honeywell TPE331)	Integrated Starter and Generator	USA	MALE
General Atomics Mojave	Single Turboprop (Rolls-Royce M250)	Integrated Starter-Generator	USA	STOL UAV
Eurodrone (MALE RPAS)	Twin Turboprop (GE Catalyst)	Integrated Starter and Generator	Germany/France /Italy/Spain	MALE
BAE Systems Mantis	Twin Turboprop (Rolls-Royce Model 250)	Integrated Starter and Generator	UK	MALE/HALE

In addition, the use of PM machines in starter generator systems is increasing, especially due to their high power density and efficiency. PM machines have the capacity to produce more power in smaller volumes, but require special design and protection strategies because of the difficulties in demagnetization and failure modes.

In recent years, the use of BLDC engine-based starter generator systems has increased significantly in mild hybrid and high altitude electrical UAV projects. Compared to traditional starter and generator systems, BLDC based integrated solutions are preferred especially in small and mediumclass UAV platforms by offering advantages such as lower weight, compact design and dual functionality. Similarly, hybrid UAV systems such as Silent Falcon also have internal combustion engines. BLDC supported starter generator systems are used for electricity generation throughout the flight after

the first engine start [31, 32]. These systems have been developed to increase flight duration, improve energy efficiency and support operational flexibility, and their use has become widespread, especially in UAVs in the 5–150 kg weight range. However, in large MALE/HALE class UAVs using high power engines over 100 HP, the use of BLDC starter generator systems is still limited due to thermal management, reliability and high electrical power requirements [33]. A representative structure of the UAVs with BLDC starter generator configuration is given in Figure 1.3.

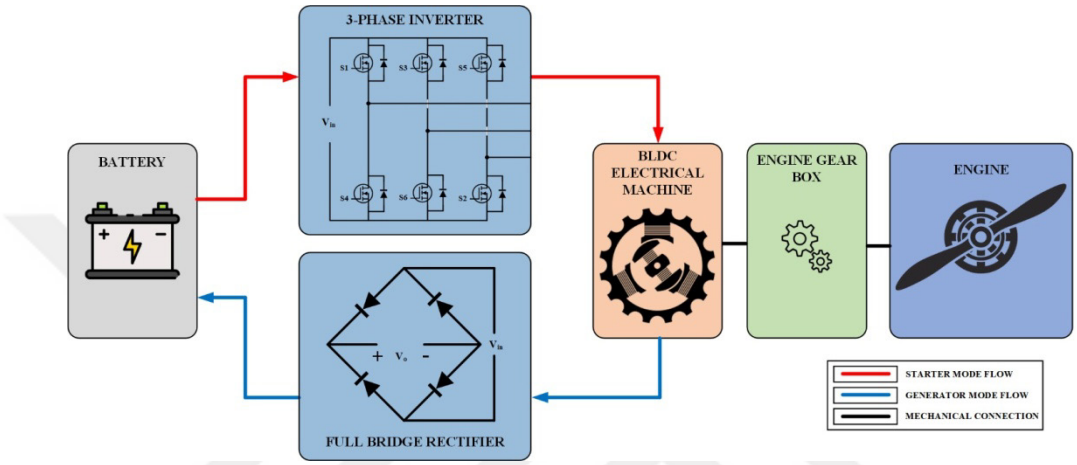

Figure 1.3 : BLDC Starter-Generator configuration of UAVs.

Operating concepts in starter and generator modes of BLDC motor based starter generator systems are derived from electromagnetic flux change. A three phase full bridge inverter converts the DC bus voltage in motor mode to AC then operates it through the stator windings. The stator's related to magnetic field produced by this current causes the rotor to rotate and produce the mechanical torque needed to start the internal combustion engine. Three phase AC electrical power is produced in generator mode when the external mechanical excitation of the rotor causes a flux shift in the stator windings, therefore producing an Electromotive Force (EMF) in the windings. This produced AC energy is converted to DC by a full wave rectifier and is used to charge batteries or supplysystem loads. While the inverter and rectifier are separate power electronics stages in traditional structures, in advanced starter generator systems, these two functions are combined by a bidirectional converter, providing high efficiency in both motor and generator modes. Thanks to these bidirectional energy conversion structures, BLDC motors offer both low volume and weight advantages and increase the flexibility of hybrid electric power systems. However, design challenges such as thermal management, reliability and efficiency must be taken into account in high power applications [32, 33].

2. PROPOSED POWER CONVERSION ARCHITECTURE

This study proposes a lightweight and efficient BLDC starter generator system suggested for UAVs. The architecture includes a FSBBC and a Three Phase Inverter to provide bidirectional power flow. The FSBB converter supports either boost or buck operation modes, optimizing voltage conversion across flight phases. The inverter drives the BLDC motor in starter mode and rectifies generated power in generator mode. A PI based control method is used to be stable voltage and current during transitions, minimizing switching losses and improving overall system performance.

2.1 Proposed BLDC Starter-Generator System Design for UAVs

In this section, a novel BLDC starter generator system specifically designed for UAVs is proposed. The proposed architecture aims to achieve efficient starter and power generation functions while minimizing weight, volume and system complexity, which are critical parameters in UAV applications. Structure of the proposed BLDC starter generator system for UAVs is given in Figure 2.1.

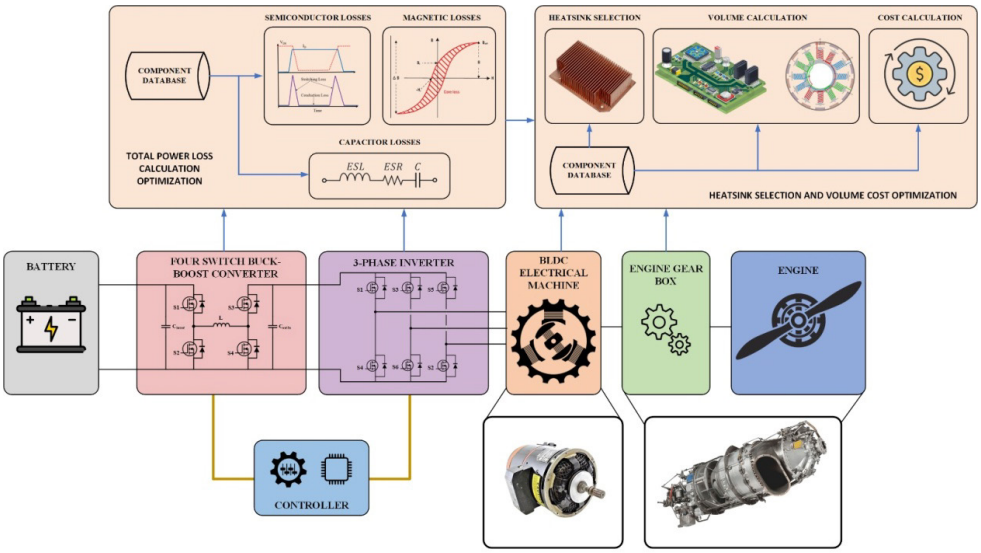

Figure 2.1 : Proposed BLDC starter generator system design for UAVs.

The proposed system design offers a lightweight and highly efficient UAV power system where the BLDC motor has both starter and generator functions. The basic components of the system consist of FSBBC and Three Phase Inverter.

FSBBC provides bidirectional energy flow between the UAV power supply and the BLDC motor. Unlike traditional unidirectional converters, this structure can operate in both boost and buck modes. During engine start, FSBBC operates in boost mode to provide the necessary voltage to the motor; in generator mode, it switches to buck mode and regulates the generated energy in accordance with the needs of the system. This four switch topology minimizes the total weight and volume of the system by reducing switching losses and the number of components, thus contributing positively to UAV performance.

The second major component of the system, the three phase inverter, operates bidirectionally: in starter mode, it converts the battery's DC voltage into three phase AC current to drive the BLDC motor; in generator mode, it rectifies the motor-generated three phase AC voltage back into DC. Utilizing a PWM based control scheme, the system enables precise and efficient regulation of both motor speed and torque.

To ensure stable and reliable operation of the overall system, a PI based control strategy is implemented for both the FSBBC and the inverter modules. This control scheme dynamically adjusts the converter duty cycles and the inverter switching sequences to regulate system voltage and current within predefined limits. Consequently, abrupt voltage transients during mode transitions are effectively mitigated, thereby enhancing system stabilitya critical factor for flight safety.

2.2 Four Switch Buck Boost Converter

The FSBBC features a circuit topology capable of operating in boost mode when the input voltage is lower than the output voltage, and in buck mode when it is higher. Unlike conventional buck boost converters, the FSBBC employs actively controlled semiconductor switches instead of passive diodes, thereby eliminating diode forward voltage losses and enhancing overall system efficiency. The FSBB diagram is given in Figure 2.2.

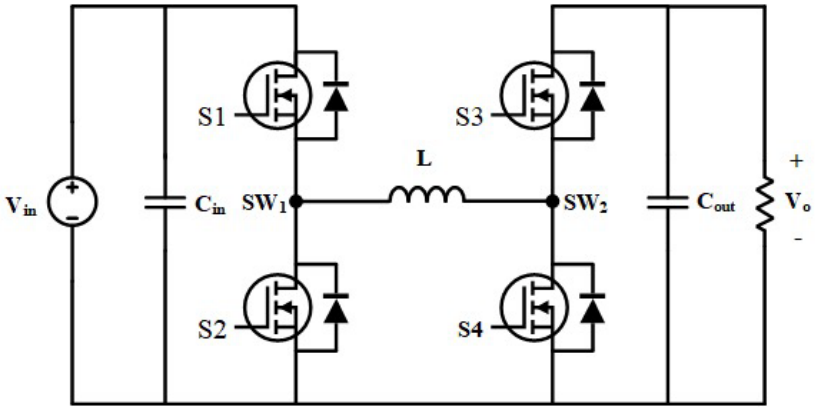

Figure 2.2 : Four switch buck boost converter.

This circuit operates in four different operating states. In buck mode, S1 and S2 operate in reverse, S3 remains in continuous conduction mode, and S4 is in cut off state. When S2 and S3 are turned on, the inductor current decreases over time and the output capacitor charges. When S1 and S3 are turned on, the source is directly connected to the load through the inductor, and the inductor begins to charge [34]. The buck operation of FSBB diagram is given in Figure 2.3.

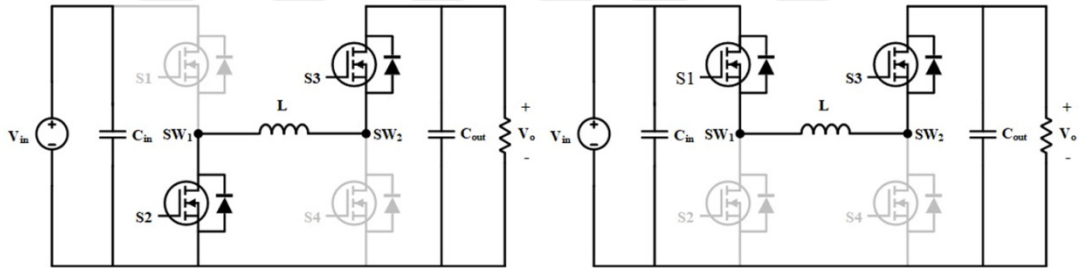

Figure 2.3 : Four switch buck boost converter buck mode operation.

In boost mode, S1 on the buck side remains in continuous conduction and S2 is in cut off mode with 0% duty cycle. S3 and S4 on the boost side operate in opposite states. In S1-S4 mode, the inductor is charged to a certain level and in S1-S3 mode, the load is fed through the inductor [34, 35]. The boost operation of FSBB diagram is given in Figure 2.4.

In FSBB converter, the switches on the left side are referred to as "buck" switches, while those on the right side are termed "boost" switches. Under ideal operating conditions, the voltage gain M of the converter, derived from the voltsecond balance on the inductor, is expressed as:

$$M = \frac{V_{out}}{V_{in}} = \frac{D_1}{1 - D_2} \tag{2.1}$$

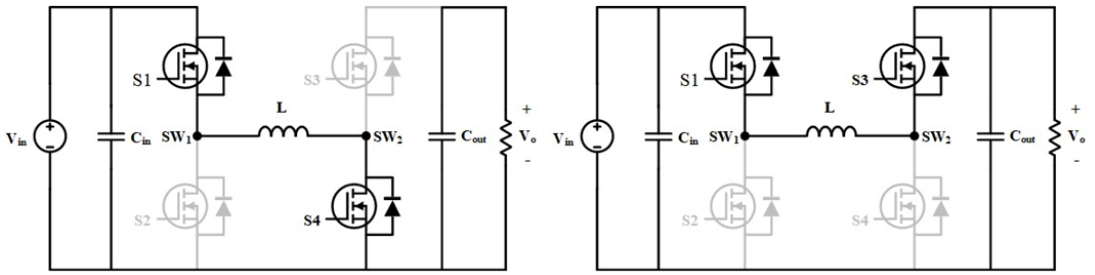

Figure 2.4 : Four switch buck boost converter boost mode operation.

Here, D_1 is the duty ratio of S_1 and D_2 is the duty ratio of S_4. In this way, the output voltage can be controlled independently via both D_1 and D_2. Various D_1-D_2 combinations are possible for the desired voltage gain.

2.3 Brushless DC Starter and Generator

BLDC motors are increasingly employed as primary drive elements in modern electromechanical systems. This widespread adoption is driven by advancements in motor drive technologies and the inherent advantages of BLDC motors, including ease of control and manufacturing, high efficiency, and the ability to deliver desired torque and speed characteristics. Structurally, a BLDC motor consists of two main components: the stator and the rotor. Owing to the presence of permanent magnets on the rotor, it operates as a synchronous machine [36].

The stator comprises coils formed by winding copper wire and electrically interconnecting them. In three phase motors, these coils are typically configured in a star (Y) connection. The spatial distribution of stator windings determines the number of poles, directly influencing the rotational speed. Motor speed is calculated based on the ratio between the phase voltage frequency and the number of poles. Two common winding techniques are employed: concentrated and distributed windings. Concentrated windings reduce ohmic losses at low speeds but may introduce harmonic distortion at higher speeds. Distributed windings, on the other hand, generate a more sinusoidal back electromotive force (EMF) and enhance efficiency by minimizing electromagnetic losses [37].

The rotating component of the motor, the rotor, incorporates permanent magnets. These magnets can be either surface mounted or interior mounted within the rotor structure. Surface mounted configurations provide higher torque density, while embedded designs offer improved mechanical robustness by protecting the magnets from centrifugal forces. The efficiency and torque capability of the motor are highly dependent on the positioning of these magnets. Additionally, the air gap between the rotor and stator plays a critical role in shaping the magnetic field distribution and torque production characteristics [38]. 3 Phase BLDC motor structure and parts are given in Figure 2.5.

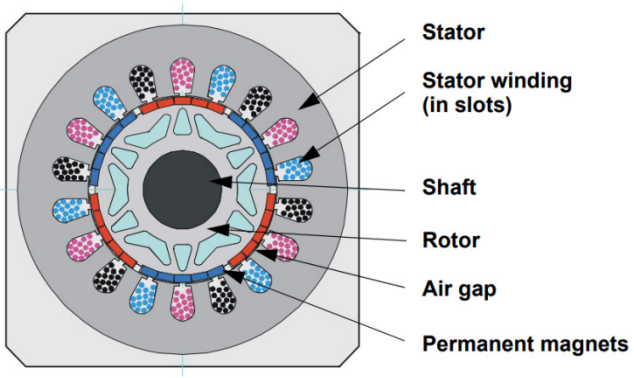

Figure 2.5 : 3-Phase BLDC motor structure and parts [39].

BLDC motors have electronic systems that control the windings that are energized according to rotor position information. Hall effect sensors, optical encoders or resolver sensors are usually used to detect the rotor position. These sensors monitor the movement of the rotor and produce logic signals to open and close the switching elements that allow the motor to rotate correctly. In this way, the motor is operated in an efficient and controlled manner. 3 Phase BLDC motor structure is given in Figure 2.6.

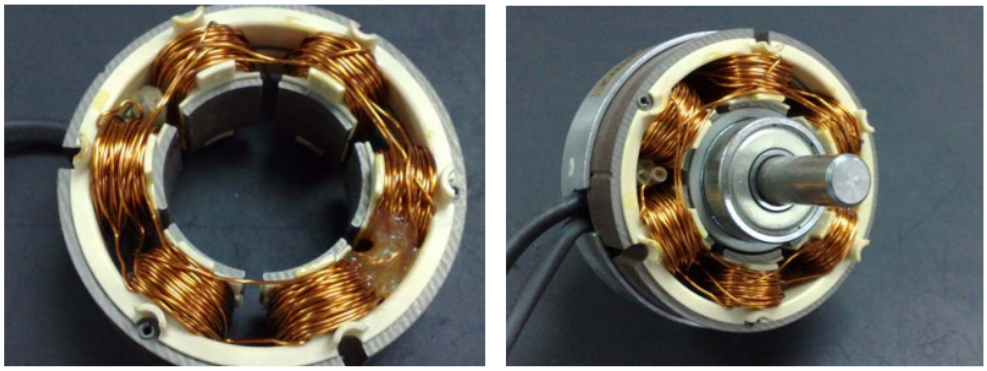

Figure 2.6 : The structure of BLDC [40].

The operating principle of a BLDC motor relies on the interactionspecifically the repulsion and attractionbetween magnetic poles. When current flows through the stator windings, it generates electromagnetic poles that interact with the permanent magnets on the rotor. The rotor magnets are repelled by stator poles of the same polarity and attracted to those of opposite polarity, generating torque and initiating rotation. By sequentially energizing the stator windings, a rotating magnetic field is produced, which sustains continuous rotation of the rotor. To maintain uninterrupted motion, the stator windings must be continuously energized in a precise sequence synchronized with the rotor position.

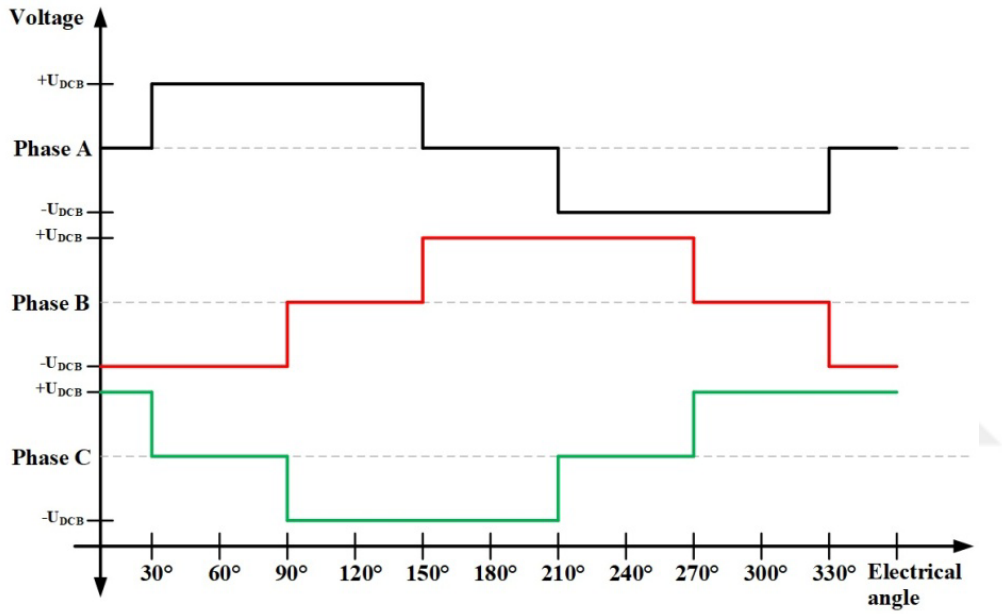

Figure 2.7 : BLDC motor phase voltages.

Inverter circuits are used to energize the windings. Inverters are circuits that convert constant DC voltage to AC voltage with the desired frequency and amplitude. Three phase inverters are used for three phase BLDC motors. There are six power switches in three phase inverters, and these switches energize the three phases of the motor in sequence. The switching signals are applied in the form of a square wave signal that determines the motor speed. Figure 2.7 illustrates the phase voltage waveforms of the BLDC motor, highlighting the typical six-step commutation pattern that produces trapezoidal back EMF characteristics and ensures efficient torque production The motor speed is proportional to the phase voltage frequency, as the frequency increases, the motor speed increases. After the switching sequence, as the motor completes its

mechanical revolution, the sensor outputs, the back EMF force, torque and phase currents are determined in a characteristic way.

BLDC motors can also operate as generators; however, the operating principle in generator mode differs from that in motor mode. In generator operation, mechanical energy is applied to the rotor, causing it to rotate. As the rotor spins, the permanent magnets create a time varying magnetic field across the stator windings. According to Faraday's law of electromagnetic induction, this changing magnetic flux induces an EMF in the stator windings, thereby generating electrical voltage.

While in motor mode the stator windings are energized to produce mechanical torque, in generator mode the rotor is driven by an external mechanical source, and the resulting motion induces voltage in the stator. This process converts mechanical energy into electrical energy. To effectively use a BLDC motor as a generator, precise control of the rotor speed is required to regulate both the generated power and system voltage. The magnitude of the generated electrical power is directly influenced by the rotor speed and the strength of the magnetic field. Additionally, accurate rotor position detection is crucial for proper commutation. This is typically achieved using Hall effect sensors or sensorless estimation algorithms to determine the correct switching sequence [41].

2.4 Six Step 3 Phase BLDC Inverter/Synchronous Rectifier

Six step commutation is a widely adopted method for controlling BLDC motors, particularly in cost sensitive and low complexity applications. This technique relies on the sequential energization of the stator windings to generate a rotating magnetic field that interacts with the rotor's permanent magnets, thereby producing torque and enabling continuous rotation. In each commutation step, two of the three motor phases are energized one with positive polarity and the other with negative while the third phase remains unpowered. This results in six discrete steps per electrical cycle, dividing the 360° electrical cycle into 60° intervals [40]. Figure 2.8 shows the six step drive approach.

This inverter topology can operate bidirectionally, enabling both motoring and generating modes. In motor mode, it functions as a three phase inverter, supplying appropriately commutated phase voltages to drive the BLDC motor. Conversely, in

generator mode, it acts as a synchronous rectifier, converting the back EMF generated by the rotating motor into DC power. This bidirectional capability is particularly advantageous in applications such as UAV starter generator systems, where the same power stage is used for propulsion and energy regeneration. As illustrated in Figure 3.8, in the six step drive approach, the selection of energized phases depends on the rotor position, which is typically determined using hall effect sensors or sensorless estimation algorithms. For example, during the first 60° segment, phase 1 and phase 2 may be energized, while phase 3 remains unpowered. This sequence advances in steps, ensuring that the magnetic field rotates in sync with the rotor position and sustains torque production throughout the cycle [42].

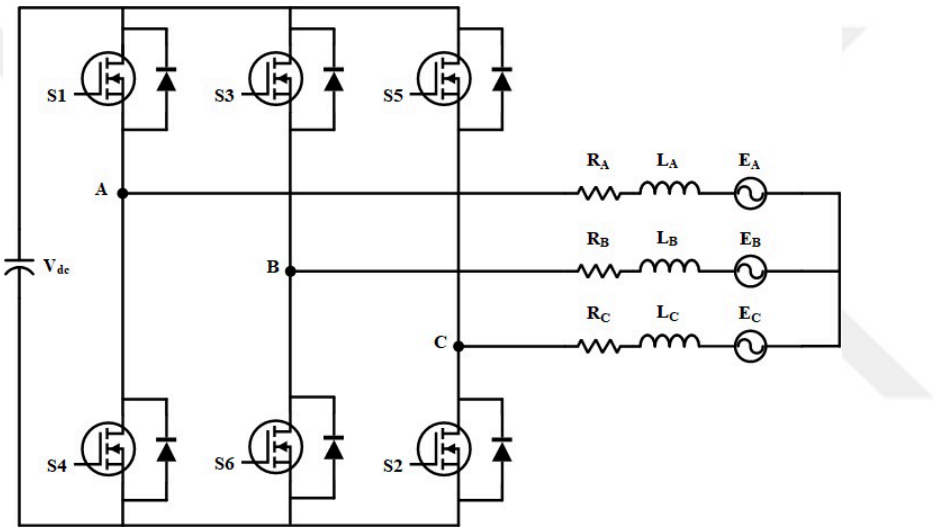

Figure 2.8 : Six step drive system for BLDC motor [42].

Each commutation event involves the operation of power switches to apply current to the stator windings with the appropriate polarity. The controlled switching not only determines the direction of rotation but also influences speed and torque. Since only two phases conduct current at any given time, the method offers a simplified switching logic and reduced computational overhead. However, this simplicity comes at the cost of increased torque ripple due to the discontinuous nature of excitation.

The back EMF produced in BLDC motors driven by this method typically exhibits a trapezoidal waveform. This waveform shape matches the six step commutation pattern and ensures efficient energy transfer between electrical and mechanical domains. Despite its limitations in precision applications, six step commutation remains a

practical and efficient solution for many motor drive systems [43]. The trapezoidal waveform is given by Figure 2.9.

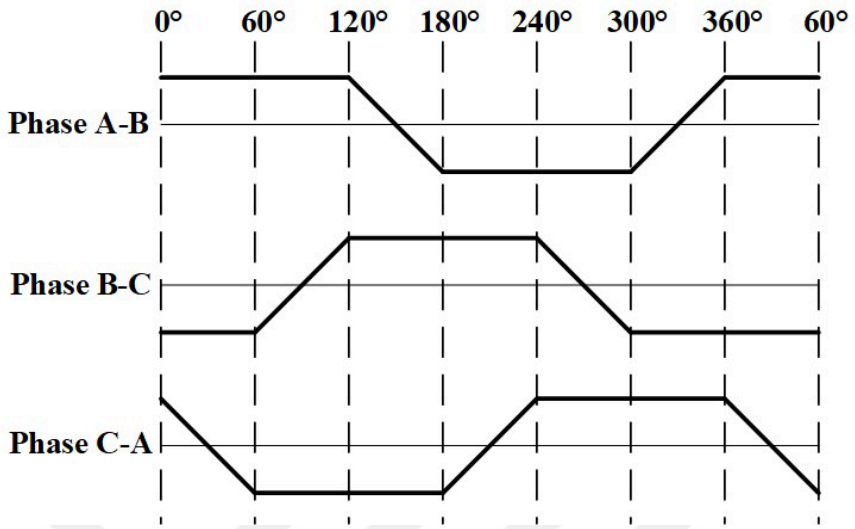

Figure 2.9 : Trapezoidal Back EMF.

2.5 Power Loss Comparison of Bidirectional Drives

In advanced BLDC motor drive systems, enabling bidirectional energy flow is essential for achieving high efficiency and system reliability, particularly in electric and hybrid vehicle applications. A commonly adopted topology in the literature involves using a single six switch full bridge inverter to facilitate both motor (starter) and generator modes of operation. As depicted in Figure 2.10, in starter mode, electrical energy is delivered from the battery to the BLDC motor via the FSBB converter and the six switch inverter, enabling motor startup and torque production. As shown in Figure 2.11, during generator mode operation, the power flow is reversed: electrical energy generated by the BLDC generator is transferred to the battery through the synchronous rectifier and the FSBB converter, enabling battery charging.

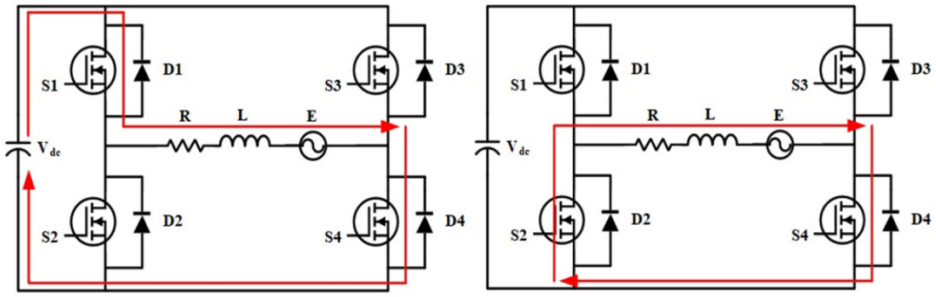

Figure 2.10 : Starter mode power flow [44].

In this system, sensorless commutation is obtained from the phase to phase voltages with the help of RC filters and comparators, eliminating the need for additional sensors and ADC [44].

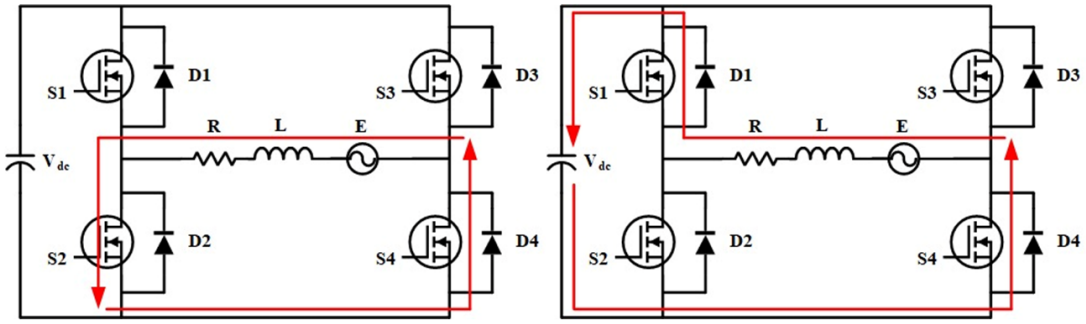

Figure 2.11 : Generator mode power flow [44].

The total power losses in this topology can be modeled as the sum of switching losses (P_{sw}), conduction losses (P_{cond}), and diode conduction losses (P_d), and are expressed as follows:

$$P_{sw} = \frac{1}{2}.V_{dc}.I_{avg}.(t_{on} + t_{off}).f_{sw} \tag{2.2}$$

$$P_{cond} = {I_{rms}}^2.R_{DS(on)} \tag{2.3}$$

$$P_d = V_f.I_{avg} \tag{2.4}$$

In a representative case, when the system delivers an average current of 5 A, and assuming a diode forward voltage drop of V_f=1 V, the power loss solely due to the diode can be calculated as P_d=5 W. If the output power is 20 W, the system efficiency with a total loss of 5 W is:

$$\eta = \frac{20}{20+5}.100\% = 80\% \tag{2.5}$$

calculated as. This result demonstrates that, particularly under generator mode operation, system efficiency can degrade to levels around 78–82%. In the alternative architecture evaluated in this study, the battery voltage is regulated by the FSBB converter prior to being delivered to the motor via a six step inverter. Since the boost functionality is performed using actively controlled switches instead of diodes, diode conduction losses are effectively eliminated, and both conduction and switching losses become more manageable. Moreover, in generator mode, the six step inverter topology functions as a synchronous rectifier. As a result, the efficiency losses typically

associated with diode conduction are significantly reduced, since power conversion is handled by actively controlled switches instead of passive diodes. In this system, for example, when $R_{DS(on)}$=20mΩ and average current I_{rms}=5A of MOSFETs, the conduction loss is:

$$P_{cond} = 5^2.(0.02) = 0.5\ W \tag{2.6}$$

In addition, assuming an average P_{sw}≈0.5W for each switching cycle, the total loss is around 1 W. In this case:

$$\eta = \frac{20}{20+1}.100\% \approx 95.2\% \tag{2.7}$$

can be calculated as. In real conditions, this efficiency can drop to 88-91% due to parasitic and nonlinear effects. These results are also consistent with experimental studies in the literature [45, 46]. Although gate losses (P_g) and reverse recovery (P_{rr}) losses are defined theoretically, these components constitute less than 1–2% of the total loss due to the low gate load capacity of the MOSFETs used in the examined system and the short reverse recovery time. Therefore, these losses are negligible in the efficiency analysis of the system.

As a result, the FSBB converter combined with the six step inverter/synchronous rectifier architecture operates with lower conduction losses and ensures more uniform thermal distribution. In this regard, it provides higher efficiency compared to conventional single stage inverter/diode rectifier topologies. In applications requiring frequent or continuous regenerative operationsuch as in UAVs the FSBB based architecture offers a more efficient and reliable solution.

2.6 Proposed System Design Simulations and Discussion

The simulation models for both starter and generator modes are presented in Figure 2.12 and Figure 2.13. In the simulation, a PMSM block from the Simulink library is used, configured with a trapezoidal Back EMF waveform to represent BLDC motor behavior.

In starter mode, the electrical power drawn from the system bus bar is converted into mechanical power, thereby providing the required drive torque to the platform. Once the system dynamics stabilize, the operation transitions into generator mode.

In generator mode, mechanical power supplied to the rotor is converted into electrical energy, which is then fed back to the system busbar, enabling energy recovery and battery charging.

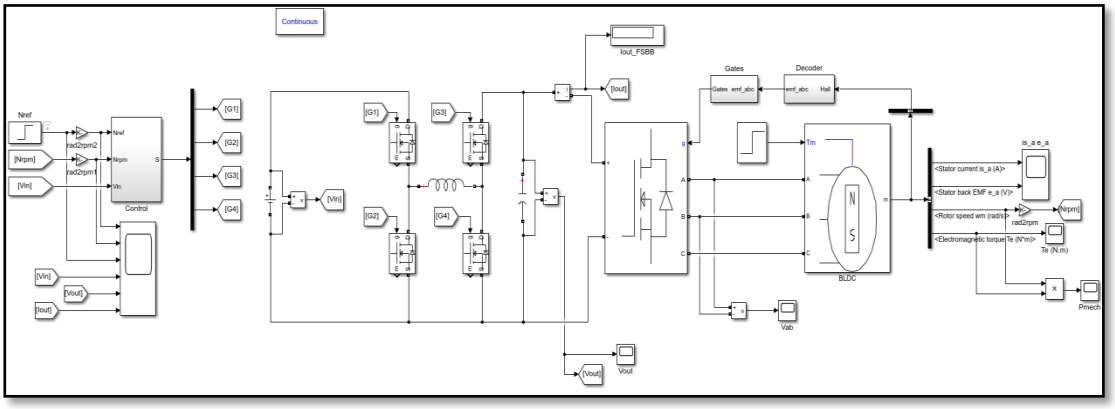

Figure 2.12 : Starter mode simulation model.

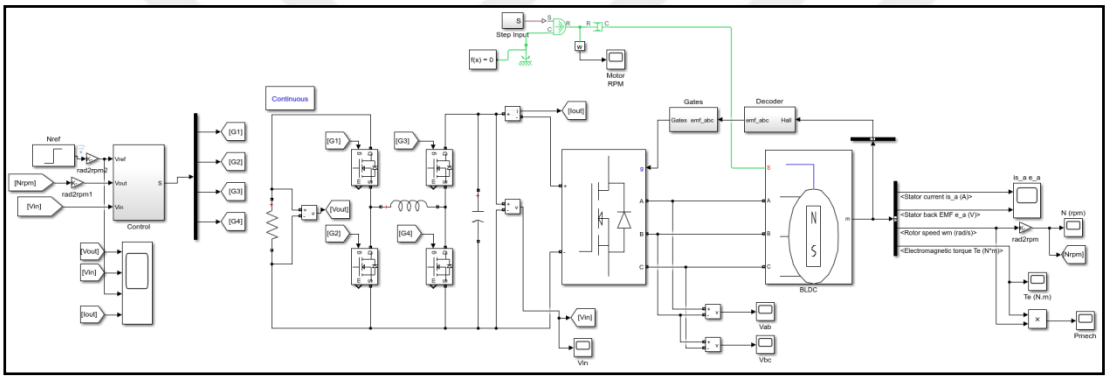

Figure 2.13 : Generator mode simulation model.

The parameters of the BLDC Starter/Generator are given in Table 2.1 and Table 2.2.

Table 2.1 : Starter mode parameters.

Parameter	Value
Voltage	48 V
Current	25 A
Nominal Speed	1500 rpm
Nominal Torque	6 Nm
Torque Constant	0.24 Nm/A
No-load Speed	2700 rpm
Efficiency	>90%

Table 2.2 : Generator mode parameters.

Parameter	Value
Voltage Range	30 V – 135 V AC
Number of Poles	2p = 14
Back-EMF Type	Sinusoidal

Parameter	Value
Voltage Constant (Ke)	16.6 Vrms/krpm
Nominal Power	1200 VA
Speed Range	1800–8000 rpm
Current Range	6–27 Arms
Terminal Resistance	18 mOhm
Terminal Inductance	37.3 µH
Nominal Efficiency	>90%

Figure 2.14 illustrates the stator phase current and voltage waveforms observed during the starter mode operation of the BLDC motor, highlighting the characteristic six step commutation pattern and the corresponding voltage transitions applied by the inverter.

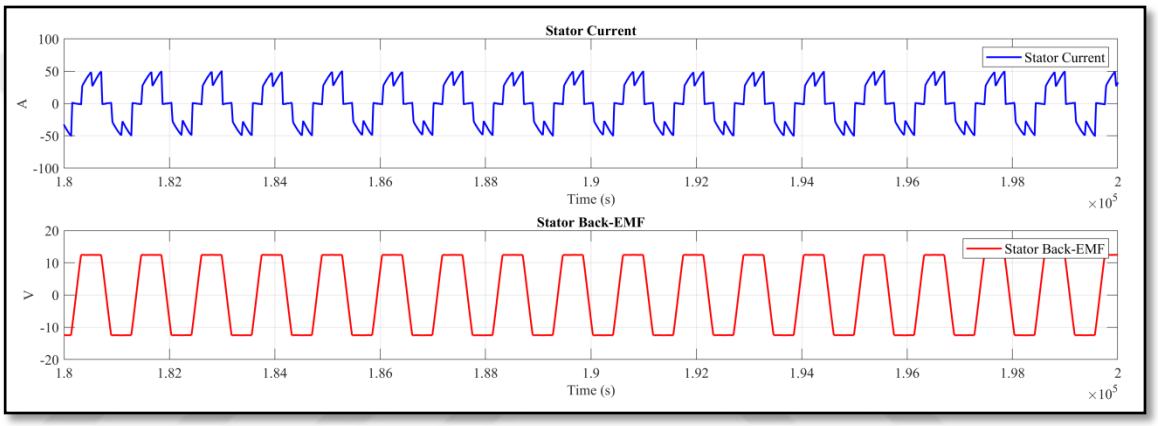

Figure 2.14 : Starter mode stator current and voltage graph.

Figure 2.15 presents the stator phase current and voltage waveforms during generator mode operation, demonstrating the back EMF driven current flow and the controlled rectification process performed by the synchronous rectifier stage.

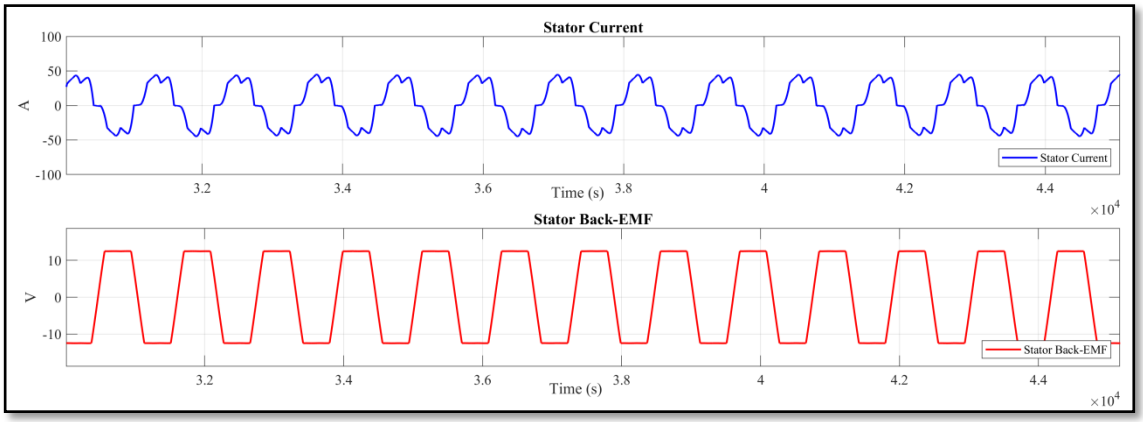

Figure 2.15 : Generator mode stator current and voltage graph.

3. SYSTEM LEVEL OPTIMIZATION FOR PROPOSED POWER SYSTEM ARCHITECTURE

This section introduces a system level optimization methodology aimed at enhancing the overall performance of the proposed power architecture. The primary objective is to select the most suitable componentssuch as power semiconductors, magnetic elements, passive parts, and thermal management unitsfrom a predefined database, subject to constraints on total volume, cost, and power loss. To achieve this, a multi objective optimization framework is utilized, which systematically evaluates the trade offs among competing design goals and identifies an optimal component configuration under specified operating conditions.

3.1 Metaheuristic Optimization Methods

Metaheuristics are generalpurpose search strategies developed to solve high-dimensional, complex, and nonlinear optimization problems. These methods, based on artificial intelligence principles, serve as alternatives to classical heuristic techniques when those methods become insufficient. They are problem independent and can be effectively applied across a broad range of engineering applications with minimal structural adjustments.

The term metaheuristic was first introduced by Glover in 1986 and is derived from the Greek word meta (meaning “beyond” or “after”) and the English word heuristic [44]. Metaheuristics are therefore often referred to as “beyond heuristics” or “advanced heuristics,” emphasizing their ability to search solution spaces more thoroughly and successfully locate global optima.

Unlike classical heuristics, which typically operate on a single candidate solution, metaheuristic algorithms explore the solution space more extensively by simultaneously evaluating a population of potential solutions. Their adaptability makes them suitable for a wide variety of problems across different engineering

domains, as they can be easily tailored via parametric tuning. Instead of providing exact solutions, they offer high quality approximate solutions within acceptable computational effort, making them particularly suitable for real world engineering problems.

Moreover, metaheuristics are especially well suited for multi objective optimization problems. Their population based structure allows them to evaluate multiple performance objectives simultaneously, as opposed to focusing on a single criterion [48, 49]. Metaheuristic algorithms can be categorized based on their underlying mechanisms and inspiration sources. A common classification distinguishes between nature inspired and non-nature-inspired approaches. Nature inspired algorithms are modeled after biological or physical processes observed in nature. For instance:

- Particle Swarm Optimization (PSO) is inspired by the flocking behavior of birds;
- Genetic Algorithm (GA) mimics natural selection and evolutionary processes;
- Ant Colony Optimization (ACO) is based on pheromone-guided pathfinding in ants;
- Firefly Algorithm (FA) models light-attracted movement of fireflies;
- Simulated Annealing (SA) is inspired by atomic annealing processes in thermodynamics [50–52].

3.2 Particle Swarm Optimization Algorithm

PSO is a population based metaheuristic algorithm inspired by the flocking foraging behavior of birds. The PSO algorithm is based on the process of determining the optimal solution by navigating the solution space according to certain guidelines for a collection of "particles" representing possible solutions. The efficiency of each particle is determined by the output of the optimized objective function. The algorithm starts with defining the basic parameters, including the maximum number of iterations and the number of particles. Each particle is guided to its new location by referring to the best solution in its past (personal best - p_{best}) and the best solution among all particles (global best - g_{best}). The speed and position updates of the particles are determined by the collective experience of the swarm and their own experience. The goal is to reach

the optimal point in the solution space, and this process is repeated until the maximum number of iterations is reached [50]. Figure 3.1 presents the flowchart of the particle swarm optimization (PSO) algorithm, illustrating the iterative process of initializing particles, evaluating fitness, updating positions and velocities, and converging toward the optimal solution.

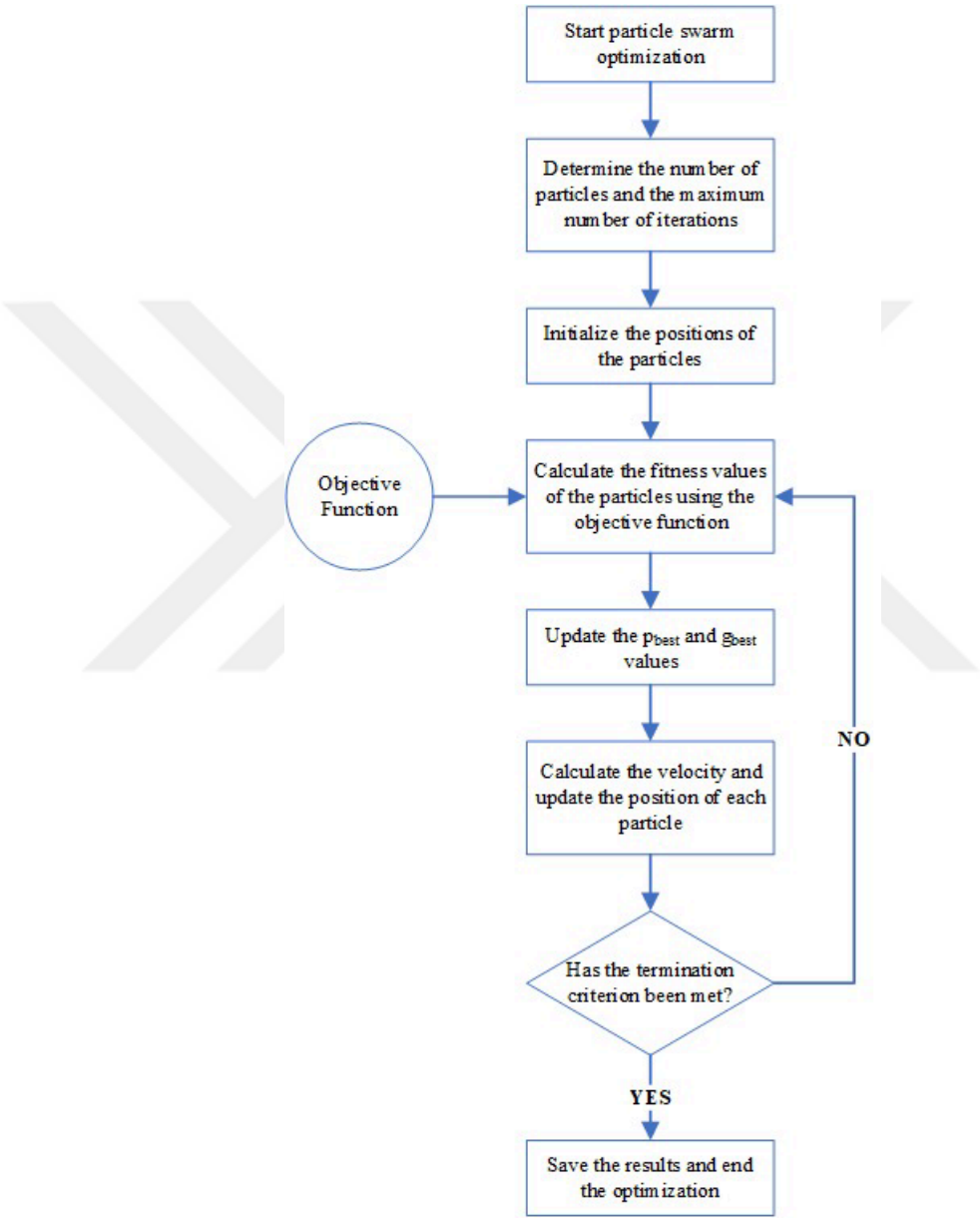

Figure 3.1 : Particle swarm optimization algorithm flowchart.

In this study, the PSO algorithm is implemented in the MATLAB environment to solve a multi criteria optimization problem. The developed code is designed to explore the solution space and identify the optimal configuration of decision variables by adhering

to the fundamental principles of PSO. The main steps of the algorithm are outlined below.

The process begins with the definition of the optimization problem and associated parameters. This includes specifying the number of decision variables (n_{Var}) and assigning their respective lower and upper bounds (V_{arMin}, V_{arMax}). Core PSO parameters such as the inertia weight (w), cognitive coefficient (c_1), and social coefficient (c_2) are initialized to control the influence of individual and collective learning behaviors on particle movement. Additionally, velocity boundaries (V_{elMin}, V_{elMax}) are defined to prevent excessive fluctuations in particle positions, ensuring more stable convergence behavior.

During the initialization phase, each particle's initial position is generated randomly within the defined search space. The objective function is evaluated for each particle, and the resulting cost values are computed. These initial solutions are recorded as each particle's personal best (p_{Best}), while the best performing particle among the swarm is selected as the global best (g_{Best}).

In each iteration of the PSO loop, the velocity and position of every particle are updated based on a combination of its personal best position and the global best position identified within the swarm. These updates enable the particles to explore promising regions of the solution space while being guided by both individual experience and collective intelligence. Following the update, the objective function is reevaluated for the new positions, and the personal and global bests are revised if improvements are detected.

To enhance convergence and avoid premature stagnation, the inertia weight (w) is gradually decreased in each iteration using a damping factor (w_{damp}). This dynamic adjustment helps balance the exploration and exploitation capabilities of the algorithm over time. Throughout the optimization process, the best cost value obtained in each iteration is recorded and stored in an array named BestCost. At the end of the process, the GlobalBest structure holds the optimal decision variable vector, while the BestCost array provides a performance trace of the algorithm across iterations.

3.3 Proposed System Design and Optimization

In recent years, power electronic systems have become one of the prominent application domains for metaheuristic optimization algorithms. The design process of power electronic converters often evolves into a highly complex optimization problem due to factors such as high frequency switching behavior, compact structural requirements, and the necessity to simultaneously consider multiple performance criteriaincluding efficiency, cost, volume, reliability, thermal constraints, and sustainability.

Under such multi faceted constraints, classical analytical design methods often become insufficient or computationally prohibitive, thereby motivating the adoption of metaheuristic approaches as effective alternatives. In this study, the PSO algorithm is employed to minimize a multi objective fitness function that accounts for total volume, cost, and power loss within the FSBB converter and six step inverter/synchronous rectifier topology designed for a BLDC starter generator system in UAV applications.

BLDC motors are extensively utilized across various sectors due to their high efficiency, compact form factor, and mechanical robustness. However, in high frequency switching conditions, substantial energy losses can arise in semiconductor switching devices particularly MOSFET swithin both the converter and inverter stages. These switching losses not only reduce the overall system efficiency but also significantly increase the burden on thermal management systems. Therefore, the optimal selection of power semiconductors, passive components, and associated control parameters becomes a critical design requirement. By leveraging PSO based optimization, this study aims to develop a power conversion architecture that is not only more energy efficient and thermally stable, but also more compact and cost effective specifically tailored to meet the stringent performance demands of BLDC starter generator systems in UAVs.

3.3.1 Loss-Cost-Volume modelling of power stage

The selection of switching devices in power stage is made from among MOSFET semiconductor switches, which are widely used in modern power electronics applications. Initially, the relevant specifications of the switches are uploaded into a component database. Using predefined evaluation functions, the most suitable switching element is selected from this database. In the algorithm, the selection process

is based on the total power loss occurring in the switching device. These losses are considered as the sum of conduction loss, switching loss, gate loss, and reverse recovery loss [53].

When calculating the conduction loss, the resistance value of the switch at the moment of conduction (R_{DSon}, Ω) and the effective value of the current passing through the switch are taken into account.This loss can be calculated by equation 3.1.

$$P_{cond} = I_{rms}{}^{2}.R_{DS(on)} \tag{3.1}$$

The switching loss can be calculated using equation 3.2 where V_{dc} denotes the voltage across the switch at the moment of turn off, I_{avg} represents the average current flowing through the switch at the moment of turn on, t_r corresponds to the rise time of the current during the switch's transition to conduction, and t_f denotes the fall time during the transition to turn off.

$$P_{sw} = \frac{1}{2}.V_{dc}.I_{avg}.(t_{on} + t_{off}).f_{sw} \tag{3.2}$$

Gate driving loss arises due to the energy dissipated when charging and discharging the parasitic capacitances at the gate terminal of a power switch during each switching event. This type of loss, known as gate loss, can be calculated using equation 3.3. In this expression, Q_g represents the total gate charge (in Coulombs) accumulated at the gate terminal, and V_{gs} denotes the maximum gate to source voltage required to fully turn on the switch. Gate loss becomes particularly significant in high frequency switching applications and in power devices with large gate charge values. As switching frequency increases, the cumulative gate energy loss also rises, potentially contributing nonnegligibly to the total system losses.

$$P_g = Q_g.V_{gs}.f_{sw} \tag{3.3}$$

Reverse recovery loss is a form of power dissipation that occurs due to the behavior of the diode connected in reverse parallel with the switch, typically integrated within the switch's semiconductor structure. This loss is described by equation 3.4, where V_{ds} denotes the voltage across the diode during recovery, and Q_{rr} represents the total reverse recovery charge conducted by the diode.Reverse recovery occurs when the diode transitions from its conducting state to the blocking state. During this brief interval, a reverse current continues to flow as stored charge carriers are removed,

resulting in energy loss. This loss can become considerable, especially under high switching frequencies, and may significantly reduce overall system efficiency. Therefore, when selecting a diode either discrete or intrinsic to the switch it is critical to consider reverse recovery characteristics, such as recovery time and charge. Minimizing reverse recovery loss is essential for ensuring efficient operation in fast switching power electronic systems.

$$P_{rr} = Q_{rr}.V_{ds}.f_{sw} \tag{3.4}$$

In each switching cycle, the output capacitance of the MOSFET is charged and discharged, resulting in a certain amount of energy loss per period. This type of loss, known as output capacitance loss, can be quantified by equation 3.5.

$$P_{coss} = \frac{1}{2}.C_{oss}.{V_{ds}}^2.f_{sw} \tag{3.5}$$

In this equation, C_{oss} represents the output capacitance of the MOSFET, which corresponds to the charge accumulation between the drain and source terminals when a voltage is applied. V_{ds} is the drain to source voltage during switching transitions, and f_{sw} is the switching frequency. The value of C_{oss} is highly dependent on the internal design and semiconductor technology of the MOSFET, and must therefore be obtained from the manufacturer's datasheet for accurate loss estimation. In high frequency switching applications, capacitive losses associated with C_{oss} can become non negligible and significantly impact system efficiency. For this reason, such losses must be carefully considered during the design and component selection phases to ensure optimal MOSFET performance and reliable power converter operation.

The total power loss occurring on the semiconductor switching componentis given in equation 3.6.

$$P_{total} = P_{sw} + P_{cond} + P_g + P_{\text{rr}} + P_{coss} \tag{3.6}$$

The cost of power semiconductors is largely driven by advanced manufacturing processes and research/development investments, while the cost of raw materials is considered negligible. The total cost of a semiconductor device can be effectively modeled based on its chip area and package type, which also determine its electrical and thermal performance.

A linear cost model expresses the chip cost as proportional to its area, using a specific price coefficient ($\sigma_{chip,x}$, €/cm²). Additionally, the packaging cost ($\Sigma_{pack,x}$) represents a fixed amount that accounts for integration and testing processes [54].

$$\Sigma_{SC} = \sigma_{chip,x}.\mathrm{A}_{chip} + \Sigma_{pack,x} \tag{3.7}$$

In the present study, the prices of semiconductor components are evaluated based on their unit costs.

In power electronic systems, ensuring the safe operating temperature of semiconductor switching devices requires an effective thermal management strategy. For this purpose, it is necessary to verify that the selected heatsink can sufficiently dissipate the power losses of each device under the given ambient temperature. This verification is achieved by determining whether the total thermal resistance between the device junction and the ambient remains within acceptable limits [54].

In this study, the required maximum thermal resistance value for each device is calculated as follows:

$$\mathrm{R}_{th,needed} = \frac{\mathrm{T}_{\mathrm{j,max}} - \mathrm{T}_{\mathrm{a}}}{\mathrm{P}_{\mathrm{loss}}} \tag{3.8}$$

Where:

- $T_{j,max}$ [°C] is the maximum allowable junction temperature of the device,
- T_a [°C] is the ambient temperature,
- P_{loss} [W] is the total power loss dissipated in the semiconductor device.

The computed $R_{th,needed}$ serves as the thermal eligibility threshold in the heatsink selection process. An algorithm developed in this study scans a predefined heatsink database and evaluates each candidate both in terms of thermal performance and volumetric efficiency to identify the most suitable solution.

In the developed algorithm, the heatsink selection process follows a structured methodology designed to ensure both thermal compliance and spatial efficiency. For heatsink entries lacking predefined volume information in the database, the total volume is dynamically calculated based on detailed geometric attributes, including fin dimensions, spacing, and the base plate area. The total volume is composed of three main components: the base plate volume, the vertical pin type fin volume, and the

horizontal strip type fin volume. The overall heatsink volume is therefore given by the following expression:

$$V_{total} = V_{base} + n_{pin}.V_{pin} + n_{strip}.V_{strip} \quad (3.9)$$

This calculation is implemented through a custom heatsink volume function and is subsequently cached to the respective entry within the heatsink database to enhance computational efficiency during iterative runs. Once volume information is updated, the thermal eligibility of each heatsink is evaluated. Specifically, the thermal resistance value R_{sa} (or R_{th} if specified under a different field name) is compared with the required thermal threshold $R_{th,needed}$. Only those heatsinks satisfying the condition $R_{sa} \leq R_{th,needed}$ are retained for further consideration [54].

Among the thermally eligible candidates, the algorithm prioritizes the heatsink with the smallest volume, thereby supporting compact system design without compromising on thermal reliability. In scenarios where no heatsink satisfies the thermal constraint, the algorithm defaults to selecting the model with the lowest thermal resistance, ensuring failsafe operation.

The cost of heatsinks generally depends on the base material used, volume, weight, and the complexity of manufacturing processes. However, analyses have shown that costs are influenced more by manufacturing complexity and volume rather than weight. This is particularly evident in hollow fin heat sinks, which are lightweight yet among the most expensive, confirming this observation.

A market study conducted on various types of aluminum heat sinks revealed a linearrelationship between cost and volume [54]. The proposed cost model is expressed in equation 3.10.

$$\Sigma_{sink} = \Sigma^{fc}{}_{sink,x} + \sigma_{sink,x} V_{sink} \quad (3.10)$$

Here, $\sigma_{sink,x}$ represents the specific cost per unit volume (€/dm³), depending on the type of heat sink, while $\Sigma_{sink,xfc}$ accounts for fixed engineering and processing costs. For the dataset analyzed, these fixed costs were found to be negligible. In this study, the prices of heatsink components are determined based on their unit prices [54].

3.3.2 Loss-Cost-Volume modelling of magnetics

The total power loss in inductors is expressed as the sum of three main components: core loss (P_{core}), direct current resistance loss (P_{DCR}), and alternating current resistance loss (P_{ACR}). This loss can be calculated by equation 3.11.

$$P_{ind} = P_{core} + P_{DCR} + P_{ACR} \tag{3.11}$$

Core loss is the loss incurred by the inductor core as a result of exposure to a magnetic field. In many cases, this value is given as measured or calculated directly by the manufacturer. However, where it is not given, it can be calculated using coefficients specific to the core material. For ferrite cores, core loss is generally expressed by the equation in 3.12.

$$P_{core} = K_1 . f^x . B^y . V_e \tag{3.12}$$

The parameters in the equation are of great importance in terms of correctly calculating the core loss. K_1 is a constant coefficient specific to the core material used and varies for each magnetic material. f represents the switching frequency and is evaluated in kHz. B represents the peak magnetic flux density in the magnetic circuit and is usually stated in kiloGauss (kG). The x and y coefficients are exponential values obtained experimentally depending on the frequency and flux density, respectively. These coefficients reflect the dynamic magnetic properties of the core material. Finally, the V_e parameter indicates the effective volume of the core (cm^3) and varies according to the core size. The K_1, x and y values for each core type are provided by the manufacturers and vary according to the material properties. The conduction loss due to direct current resistance in the inductor windings is one of the easiest losses to calculate. This loss is calculated by multiplying the effective value of the current passing through the winding with the DC resistance of the winding. This equation is calculated with the equation in 3.13.

$$P_{DCR} = {I_{rms}}^2 . R_{DCR} \tag{3.13}$$

Within the context of this equation, the term I_{RMS} represents the effective value of the current that is flowing through the inductor in amperes, while the term R_{DCR} represents the direct current resistance of the inductor winding represented in ohms. The inductor's conduction loss can be calculated by multiplying these two quantities

together. Due to the fact that this loss is instantly converted into heat, the overall efficiency of the system is decreased, and the cooling demand is increased, which necessitates a more complex thermal management system. As a result, it is essential to give preference to inductors that have low DC resistance (DCR) values, particularly in applications that involve significant current carrying. This is because it is essential to reduce power losses while also constructing the system in a more compact and efficient manner [55].

$$P_{ACR} = I_{rms}{}^{2}.R_{ACR} \tag{3.14}$$

In equation 3.14, I_{RMS} expresses the effective value of the alternating current component passing through the inductor in amperes; R_{ACR} is the resistance of the inductor winding to the alternating current and is expressed in ohms. The product of these two parameters constitutes the AC transmission loss that occurs in high-frequency applications. This loss increases with the current passing only through the outer part of the wire, especially due to the skin effect and proximity effect, and is converted into heat, making both thermal management of the system difficult and reducing its efficiency. Although AC losses are generally negligible in low frequency applications, they become a significant loss component in systems operating at high frequencies [55].

In addition to the loss mechanisms, the cost of the inductor also plays a critical role in system level design, particularly in power constrained or weight sensitive applications such as aerospace and electric mobility. Due to the high share of material usage and manual labor in inductor manufacturing, their cost structure significantly differs from that of semiconductorbased components.

In this study, the total direct cost of an inductor $\Sigma_L{}^{dc}$ is modeled as the sum of three primary components: core, winding, and labor costs, as shown in equation 3.15:

$$\Sigma^{dc}{}_{L} = \Sigma_{core} + \Sigma_{wdg} + \Sigma_{lab} \tag{3.15}$$

- Σ_{core}: Core cost, which includes both fixed tooling expenses and the weight-based cost of magnetic core material,
- Σ_{wdg}: Winding cost, covering the cost of copper wire and associated structural parts (e.g., terminals, coil formers),

- Σ_{lab}: Labor cost, generally based on the winding weight and assembly complexity.

These subcosts are further detailed as follows:

$$\Sigma_{core} = N_{stack}.\Sigma^{fc}{}_{core,x} + \sigma_{core,x}.W_{core} \quad (3.16)$$

$$\Sigma_{wdg} = \Sigma^{fc}{}_{wdg,x} + \sigma_{wdg,x}.W_{wdg} \quad (3.17)$$

$$\Sigma_{lab} = \Sigma^{fc}{}_{lab} + \sigma_{lab,x}.W_{wdg} \quad (3.18)$$

Here, N_{stack} represents the number of stacked core elements, Σ_{fc} denotes the fixed manufacturing costs (such as for tooling, coil formers, connectors), σ terms refer to the specific cost per unit weight depending on material type, and W represents the weight of either the core or winding.

The values for σand Σ_{fc} are typically obtained from magnetic component manufacturers and vary according to material types (ferrite, iron powder, amorphous) and production scales. For large minimum order quantities, manufacturing is typically outsourced to cost effective regions, and tooling costs can be amortized and neglected in early estimations [54].

This cost model, adapted from enables the joint optimization of both loss and cost metrics. It allows the evaluation of economic trade offs between different core and winding configurations. In high volume production scenarios, the use of such a model ensures that improvements in efficiency are achieved without compromising on cost effectiveness [54].

3.3.3 Loss-cost-volume modelling of capacitors

The ripple current passing through the internal resistance of the output capacitors causes thermal loss. This loss is especially important in converters with high ripple current. Although capacitors are ideally considered as passive elements that only store and discharge energy, in reality they contain a certain equivalent serial resistance (ESR) in their internal structure. This ESR results in the power loss converted into heat due to the alternating current passing through the capacitor and this loss is called P_{cap}. This loss is expressed by the equation 3.19.

$$P_{cap} = I_{cap}{}^{2}.R_{ESR,cap} \quad (3.19)$$

In DC-DC converters with significant current ripple and in applications running high frequencies, these losses are particularly crucial. The heat on the capacitance rises with increasing ESR, therefore shortening the life time of the capacitor and lowering system efficiency. Low ESR valuesthat of ceramic or low ESR electrolytics are therefore favored as capacitors.

The most commonly used capacitor types in the field of power electronics are aluminum electrolytic capacitors and metallized polypropylene film capacitors. These two capacitor technologies differ not only in terms of their electrical characteristics but also in the way their unit prices depend on nominal ratings. The unit cost of aluminum electrolytic capacitors is primarily related to the stored energy**,** that is, proportional to $C_r V_r^2$. In contrast, for polypropylene film capacitors, the unit cost scales linearly with the capacitance C_r and rated voltage V_r.

This pricing behavior in film capacitors is explained by manufacturers as a consequence of the lower production cost of thicker film layers, which are used for higher voltage ratings. This trend generally applies to voltage levels up to approximately 2–3 kV. As a result, the costper unit of stored energy decreases with increasing voltage for film capacitors, offering more cost effective solutions at the system level.

In this study, the capacitor database consists exclusively of aluminum electrolytic capacitors**.** The cost model used for aluminum electrolytic capacitors is defined as follows:

$$\Sigma_{Al-e} = b_{Al-e}.V_r + c_{Al-e}.C_r.{V_r}^2 \tag{3.20}$$

- $b_{Al\text{-}eb}$: Voltage dependent fixed cost coefficient
- $c_{Al\text{-}ec}$: Energy based cost coefficient defined by the product of capacitance and voltage.

This structure enables capacitor selection to be evaluated not only in terms of electrical suitability but also in line with economic optimization objectives, thereby supporting more informed and cost effective design decisions at the system level.

3.4 Determination of the fitness function

In this study, a design optimization was performed under efficiency, volume, and cost constraints in the FSBB and six step inverter/synchronous rectifier for the determined input and output sizes. The objective function used during the optimization utilizes the total losses occurring in the FSBB and the six step inverter/synchronous rectifier. In addition to these, inductors, capacitances, and heatsinks in the database are also included in the objective function used for optimization.

The value that minimizes the objective function can be determined as the optimum design. In this part, V_{FET} represents the volume of the selected switch, V_{FET_best} best represents the highest volume value from the switches in the database, C_{FET} represents the cost of the selected switch, C_{FET_best}, best represents the highest cost value from the switches in the database, P_{FET} represents the total power loss of the selected switch for the relevant frequency, and P_{FET_best}, best represents the highest power loss value from the switches in the database for the relevant frequency. In order to select the switching element, inductor, and capacitance that provides the most optimum solution, each calculated value is normalized and included in the objective function. Equation 3.21, equation 3.22, equation 3.23, and equation 3.24 present the normalized expressions of volume, cost, and loss for each component, which are then weighted and aggregated to evaluate the overall performance of each candidate configuration in the optimization process.

$$f_{opt,FET} = \left(\alpha_1 . \frac{V_{FET}}{V_{FET,best}}\right) + \left(\beta_1 . \frac{C_{FET}}{C_{FET,best}}\right) + \left(\gamma_1 . \frac{P_{FET}}{P_{FET,best}}\right) \tag{3.21}$$

$$f_{opt,ind} = \left(\alpha_1 . \frac{V_{ind}}{V_{ind,best}}\right) + \left(\beta_1 . \frac{C_{ind}}{C_{ind,best}}\right) + \left(\gamma_1 . \frac{P_{ind}}{P_{ind,best}}\right) \tag{3.22}$$

$$f_{opt,cap} = \left(\alpha_1 . \frac{V_{cap}}{V_{cap,best}}\right) + \left(\beta_1 . \frac{C_{cap}}{C_{cap,best}}\right) + \left(\gamma_1 . \frac{P_{cap}}{P_{cap,best}}\right) \tag{3.23}$$

$$f_{opt,heatsink} = \left(\alpha_1 . \frac{V_{heatsink}}{V_{heatsink,best}}\right) + \left(\beta_1 . \frac{C_{heatsink}}{C_{heatsink,best}}\right) + \left(\gamma_1 . \frac{P_{heatsink}}{P_{heatsink,best}}\right) \tag{3.24}$$

The symbols α, β and γ given in the equations represent the switch, inductor, capacitor and heatsink coefficients in the objective functions of the switch, inductor, capacitor

and heatsink elements. The weight coefficients betweenv olume, cost and efficiency are adjusted by changing the coefficients. If the volume size is given more importance than other quantities, the α coefficient should be greaterthan the β and γ coefficients. If the cost size is given more importance than other quantities, the β coefficient should be greater than the α and γ coefficients. If the efficiency size is given more importance than other quantities, the γ coefficient should be greater than the α and β coefficients. A single objective function is obtained by combining the optimization objective equations expressed for the switch, inductor, capacitor and heatsink. Equation 3.25 defines the overall system objective function $f_{opt,system}$, which is formulated as the sum of the individual objective function values associated with each key component in the power stage.

$$f_{opt,system} = \left(f_{opt,FET}\right) + \left(f_{opt,ind}\right) + \left(f_{opt,cap}\right) + \left(f_{opt,heatsink}\right) \tag{3.25}$$

Through design optimization within a specified frequency range, the optimization algorithm performs circuit design by utilizing each componentswitch, inductor, capacitor, and heatsink selected from the database based on their design parameters. The fitness function employed in the optimization process aims to identify the most advantageous design in terms of volume, cost, and power loss. As a result, a circuit with high power density, low cost, and reduced volume is achieved.

Figure 3.2 illustrates the flowchart of the proposed optimization algorithm, outlining the sequential steps involved in component selection, loss evaluation, normalization, objective function calculation, and identification of the optimal design configuration.

For thermal management purposes, the UB series pin-fin heat sinks from Alpha Novatech Inc. were selected. This series, ranging from UB30 to UB50, offers a wide range of thermal performance due to variations in pin height, diameter, spacing, and base thickness.

As switching components, MOSFETs based on Si, GaN, and SiC technologies were selected. These MOSFETs, supplied by manufacturers such as Infineon, Nexperia, ON Semiconductor, Vishay, ST Microelectronics, ROHM, United SiC, Transphorm, EPC, and GaN Systems, offer a broad range of voltage ratings (60 V to 750 V) and current ratings (26 A to 156 A), thereby covering a wide variety of application scenarios. All devices are available in standard power electronics packagessuch as TO-220, TO-263,

D²PAK, and SOT-404providing mechanical diversity suitable for system-level integration.

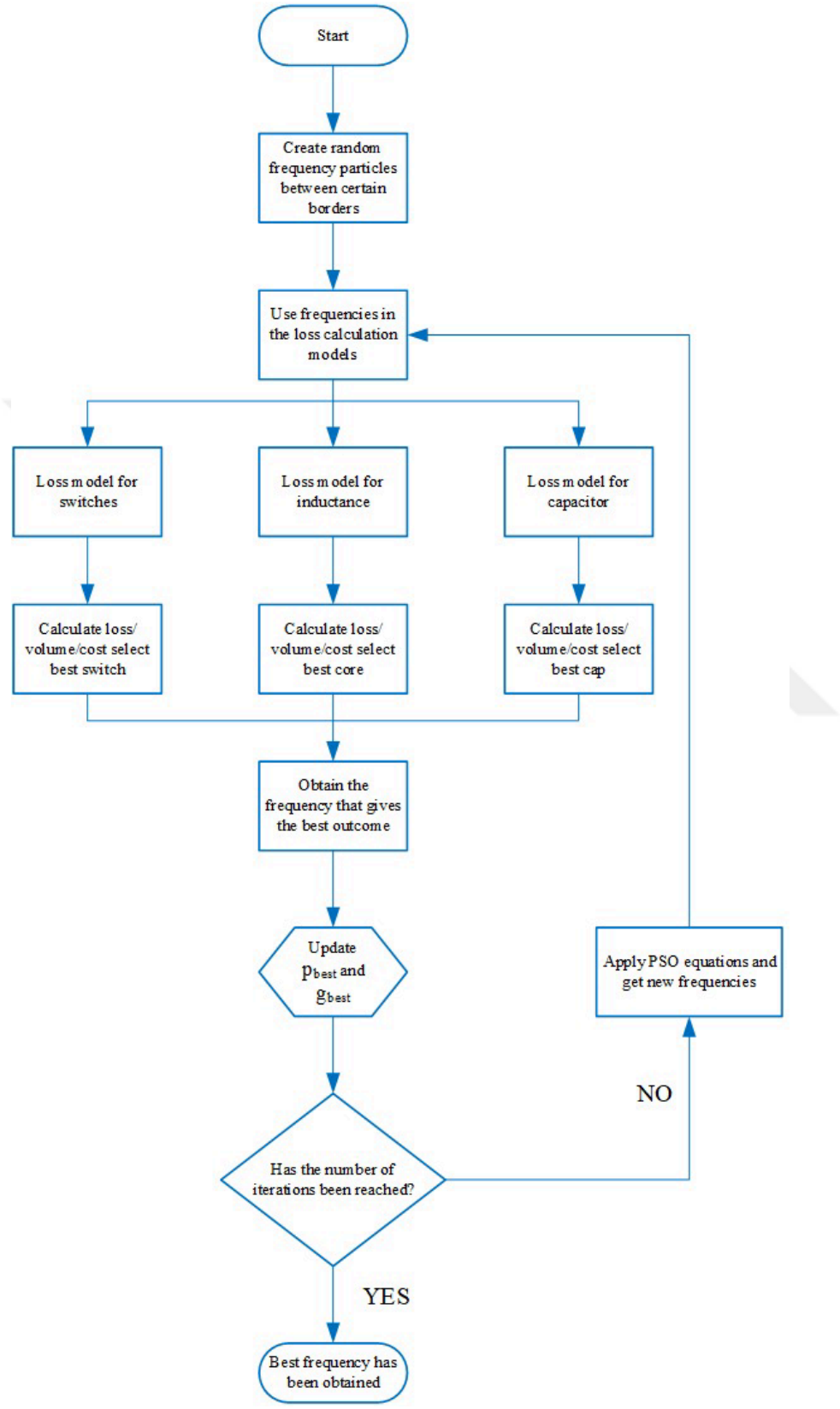

Figure 3.2 : Proposed algorithm flowchart.

This inductor database comprises models featuring E-series ferrite core geometries that are commonly used in power electronics applications. It is based on industry-recognized magnetic structures from leading manufacturers such as EPCOS (TDK), Ferroxcube, and Würth Electronic.

The capacitor database is constructed based on low-ESR and compact-volume electrolytic capacitor models from widely preferred manufacturers in power electronics applications, including Panasonic, Nichicon, Rubycon, United Chemi-Con, and Würth Electronic.

Based on the theoretical calculations presented in the previous section, three different designs were carried out under constraints of volume, cost, and efficiency. The results of each design were presented and analyzed separately.

3.5 Optimization Results

3.5.1 Volume constrainted optimization

The volume constraint is defined based on the combined volume of the inductor, capacitor, and heatsink. In the algorithm, the weighting factors of the fitness function are selected as 10% for efficiency, 80% for volume, and 10% for cost. As a result of the design optimization, the optimal fitness function value is obtained as 0.0792, with the corresponding optimal switching frequency determined to be 362 kHz. At this operating point, the converter achieves an efficiency of 97.3%, and the total cost is calculated to be $48.29.

The results of the FSBB and three phase inverter design, optimized using the PSO algorithm, are analyzed and presented.

Table 3.1 : Optimum switch parameters under volume constraints.

Switch	Conduction Loss (W)	Switching Loss (W)	Gate Loss (W)	Reverse Recorvery Loss (W)	Total Loss (W)
IRLB8721	10.7	14.9	0.23	0	25.9

Table 3.2 : Optimum capacitor parameters under volume constraints.

Capacitor	ESR Loss (mW)	Coss Loss (W)	Total Loss (W)
UCD2A220MNL1GS	7.4	0.99	0.997

Table 3.3 : Optimum inductor parameters under volume constraints.

Inductor	DC Copper Loss (mW)	AC Copper Loss (W)	Core Loss (mW)	Total Loss (W)
E-20/10/6	452	24.7	0.5	0.477

Table 3.4 : Optimum heatsink parameters under volume constraints.

Hetsink	Surface Area (cm^2)	Volume (cm^3)	Number of Fins
UB1010B	9.58	0.43	5

For each switching frequency, the corresponding switch, capacitor, inductor, and heatsink components are evaluated in terms of volume, cost, and power losses, and the most optimal components are selected accordingly. As a result of the optimization, the IRLB8721 is chosen as the switching device, E-20/10/6 as the inductor, UCD2A220MNL1GS as the capacitor, and the UB1010B as the heatsink. Figures 3.3, 3.4, and 3.5 respectively present radar charts illustrating the power loss of the selected switch, inductor, and capacitor components in the FSBB and three-phase inverter architecture. Among all components, the highest power loss is observed in the switches, while the lowest occurs in the inductor. The switching losses are significantly dominant compared to other types of losses.

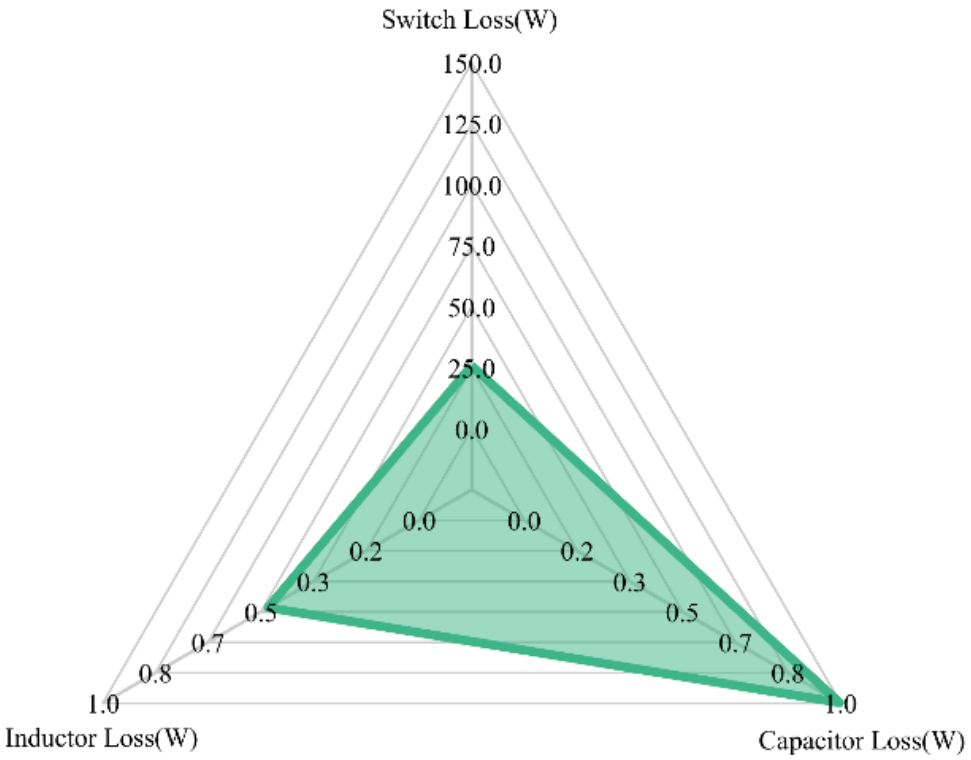

Figure 3.3 : Total losses of the volume constrained design.

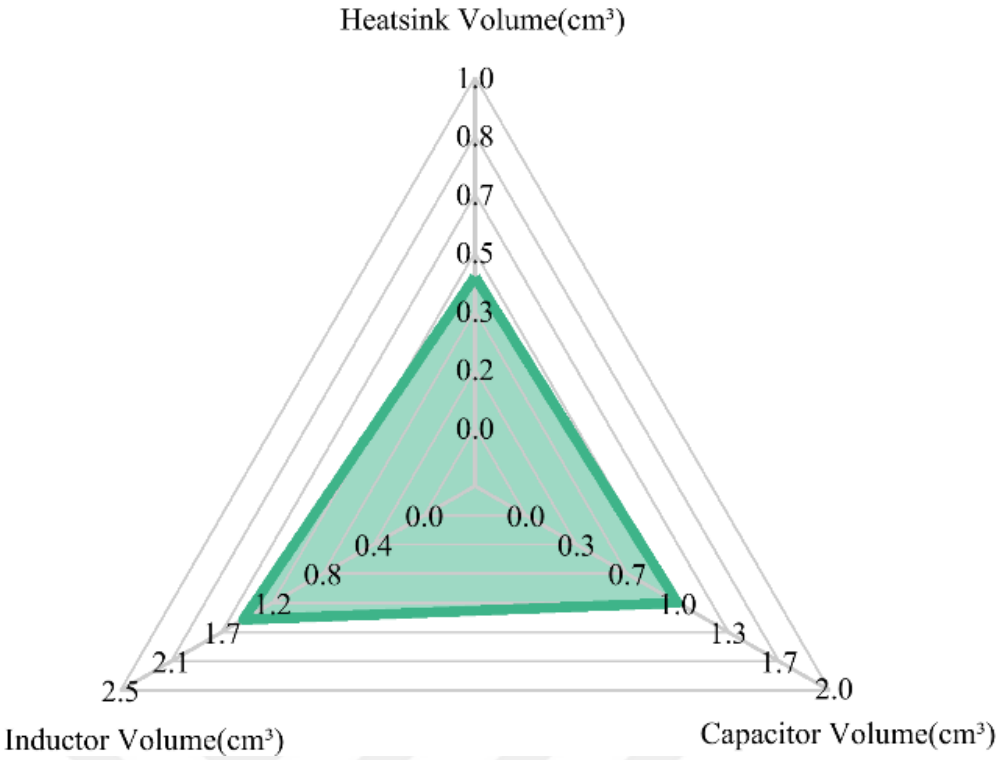

Figure 3.4 : Total volume of the volume constrained design.

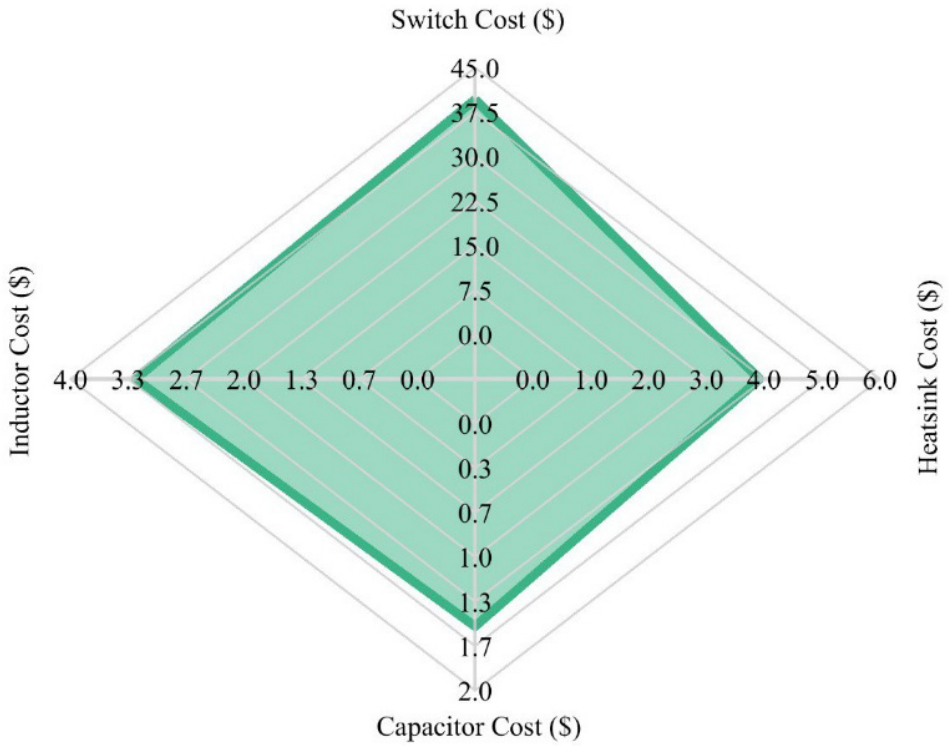

Figure 3.5 : Total cost of the volume constrained design.

3.5.2 Cost constrainted optimization

The cost constraint is defined based on the combined cost of the switch, inductor, capacitor, and heatsink. In the optimization algorithm, the weighting factors of the

fitness function are set to 10% for efficiency, 10% for volume, and 80% for cost. As a result of the design optimization, the optimal fitness function value is obtained as 0.15, with the corresponding optimal switching frequency determined to be 174 kHz. At this operating point, the converter achieves an efficiency of 92.01%, and the total cost is calculated to be $11.55

This study presents and analyzes the results of the FSBB and three phase inverter design optimized via the PSO algorithm.

Table 3.5 : Optimum switch parameters under cost constraints.

Switch	Conduction Loss (W)	Switching Loss (W)	Gate Loss (W)	Reverse Recorvery Loss (W)	Total Loss (W)
BUK9640-100A,118	46.5	51.2	0. 35	4.3	104.2

Table 3.6 : Optimum capacitor parameters under cost constraints.

Capacitor	ESR Loss (mW)	Coss Loss (W)	Total Loss (W)
EEU-FM1H101B	5.4	1.02	0.78

Table 3.7 : Optimum inductor parameters under cost constraints.

Inductor	DC Copper Loss (mW)	AC Copper Loss (W)	Core Loss (mW)	Total Loss (W)
E-22/15/6	501	19	0.3	0.520

Table 3.8 : Optimum heatsink parameters under cost constraints.

Hetsink	Surface Area (cm^2)	Volume (cm^3)	Number of Fins
UB1010B	9.58	0.43	5

For each switching frequency considered in the design process, the corresponding switch, capacitor, inductor, and heatsink components are evaluated in terms of volume, cost, and power losses, and the most optimal components are selected accordingly. As a result of the optimization, the BUK9640-100A,118 is selected as the switching device, E-22/15/6 as the inductor, EEU-FM1H101B as the capacitor, and UB1010B as the heatsink. Figures 3.6, 3.7, and 3.8 respectively present radar charts of the power loss for the selected switch, inductor, and capacitor within the optimized FSBB and three phase inverter architecture. Among all components, the highest power loss occurs in the switching devices, while the lowest is observed in the capacitor. As a

result of optimization, the switching losses are significantly dominant over other types of losses.

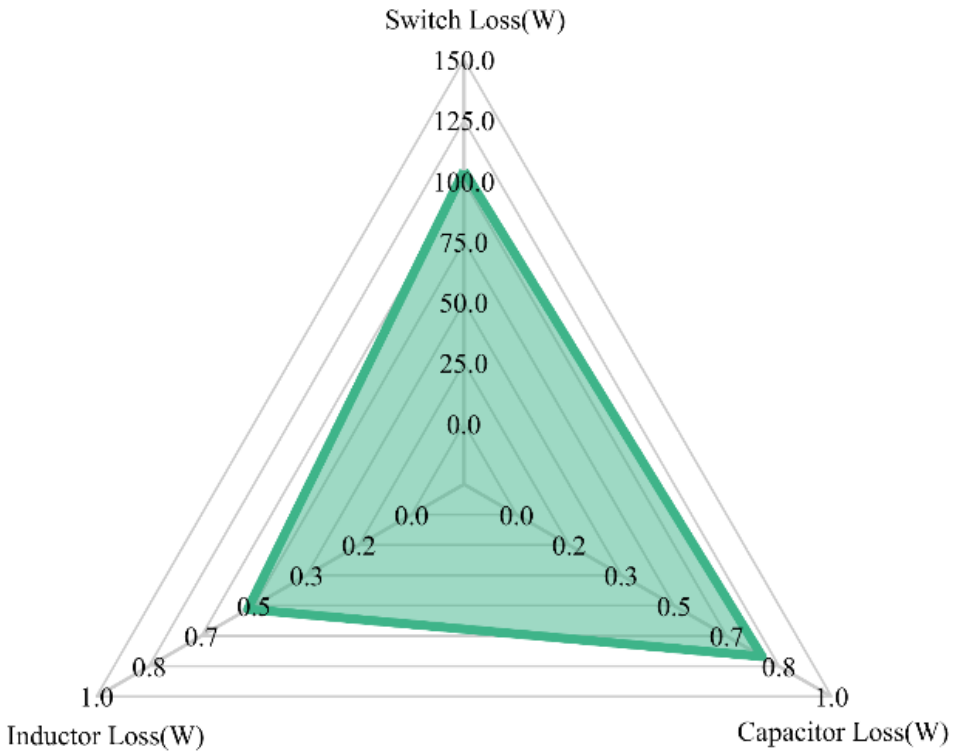

Figure 3.6 : Total losses of the cost constrained design.

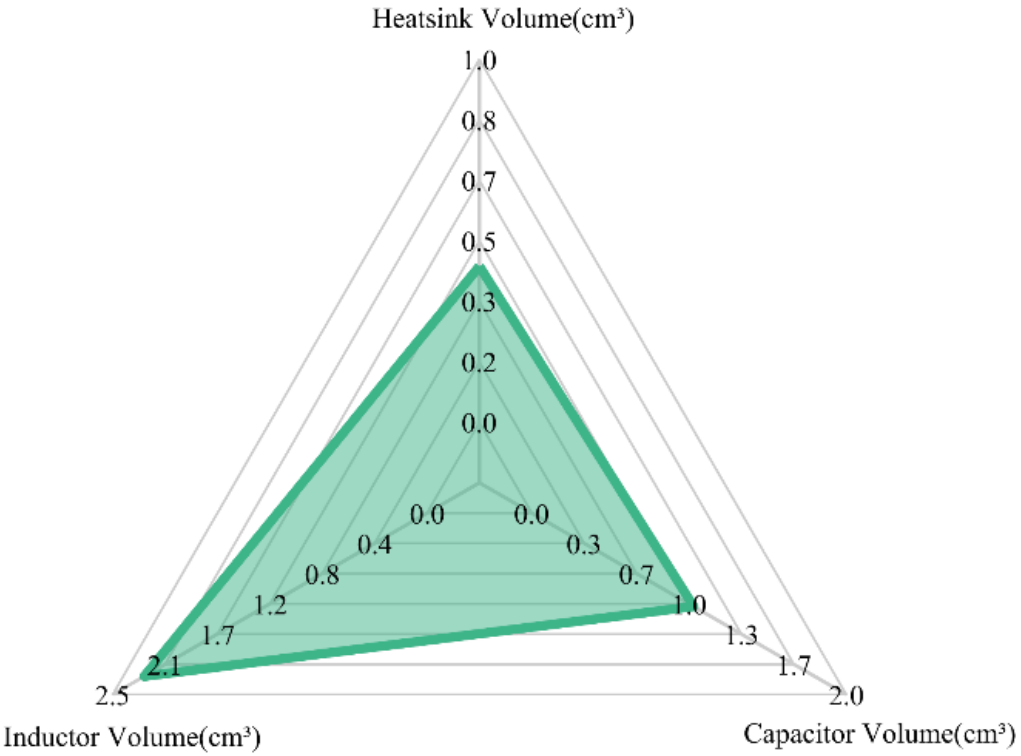

Figure 3.7 : Total volume of the cost constrained design.

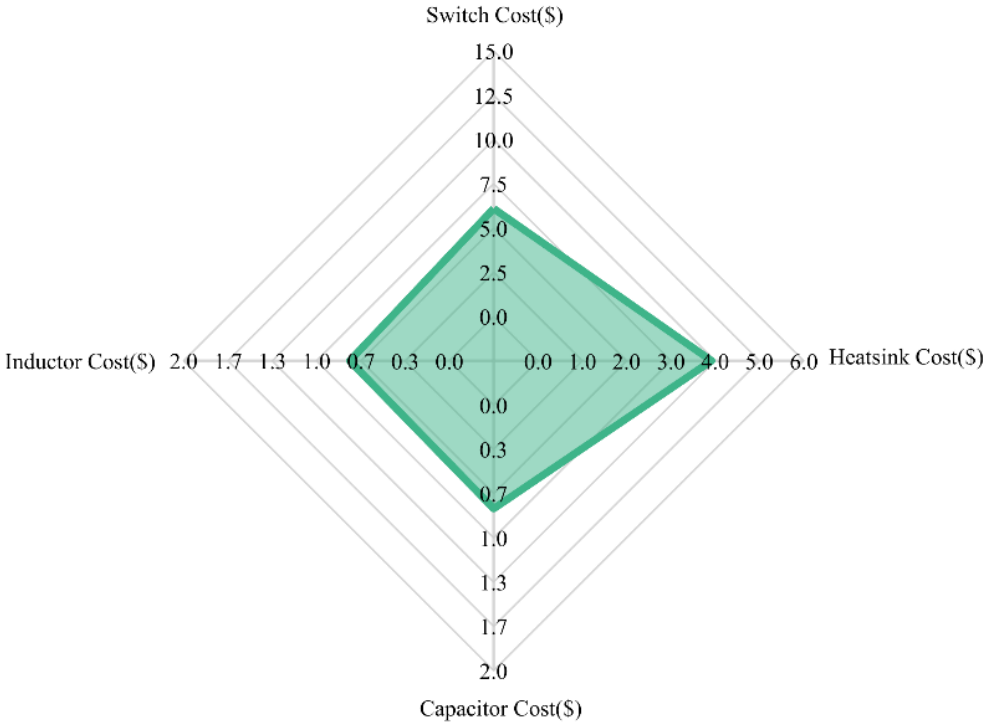

Figure 3.8 : Total cost of the cost constrained design.

3.5.3 Efficiency constrainted optimization

The efficiency constraint is defined based on the combined volume of the switch, inductor, and capacitor. In the optimization algorithm, the weighting factors of the fitness function are selected as 80% for efficiency, 10% for volume, and 10% for cost. As a result of the design optimization, the optimal fitness function value is obtained as 0.12, with the corresponding optimal switching frequency determined to be 136 kHz. At this operating point, the converter achieves an efficiency of 98.95%, and the total cost is calculated to be $17.17.

The results of the FSBB and three phase inverter design, optimized using the PSO algorithm, are examined and presented.

Table 3.9 : Optimum switch parameters under efficiency constraints.

Switch	Conduction Loss (mW)	Switching Loss (W)	Gate Loss (W)	Reverse Recorvery Loss (W)	Total Loss (W)
IRF2804	3.32	7.46	0.98	0	11.8

Table 3.10 : Optimum capacitor parameters under efficiency constraints.

Capacitor	ESR Loss (mW)	Coss Loss (W)	Total Loss (W)
UCD2A220MNL1GS	2.8	0.374	0.376

Table 3.11 : Optimum inductor parameters under efficiency constraints.

Inductor	DC Copper Loss (mW)	AC Copper Loss (W)	Core Loss (mW)	Total Loss (W)
E-22/15/6	501	16.8	0.2	0.502

Table 3.12 : Optimum heatsink parameters under efficiency constraints.

Hetsink	Surface Area (cm^2)	Volume (cm^3)	Number of Fins
UB1010B	9.58	0.43	5

For each evaluated switching frequency, the corresponding switch, capacitor, inductor, and heatsink components are analyzed in terms of volume, cost, and power losses, and the most optimal components are selected accordingly. As a result of the optimization, the IRF2804 is selected as theswitching device**,** E-22/15/6 as theinductor, UCD2A220MNL1GS as the capacitor, and UB1010B as the heatsink. Figures 3.9, 3.10, and 3.11 respectively present radar charts of the power loss forth switch, inductor, and capacitor component swithing the optimized FSBB and three phase inverter architecture. Among all components, the highest power loss occurs in the switching devices, while the lowest is observed in the capacitor. It can be noted that the switching loss is significantly dominant compared to the loss components.

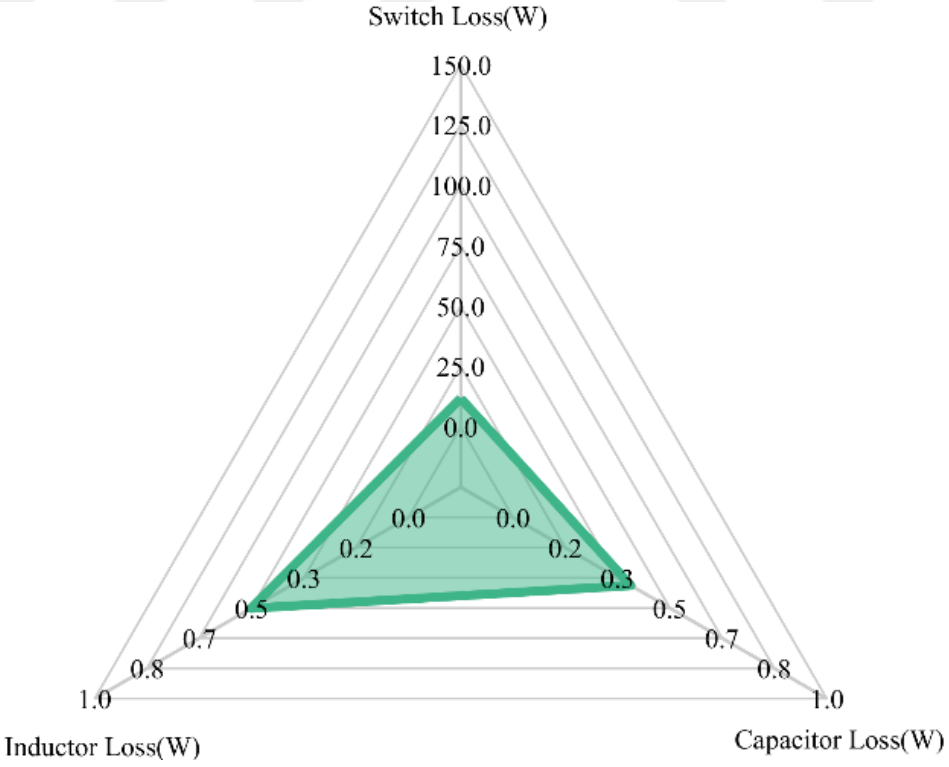

Figure 3.9 : Total losses of the efficiency constrained design.

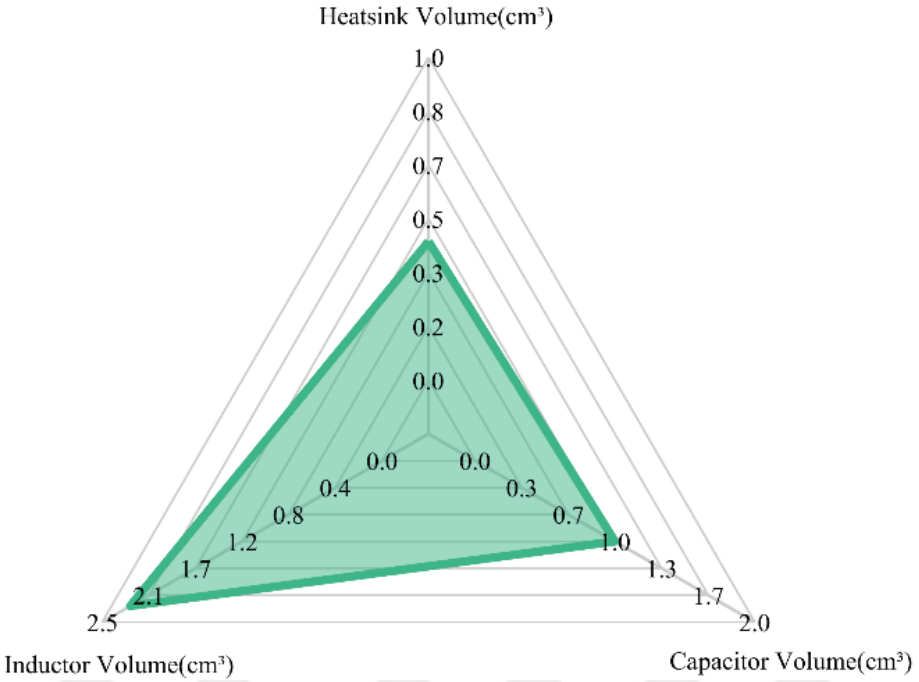

Figure 3.10 : Total volume of the efficiency constrained design.

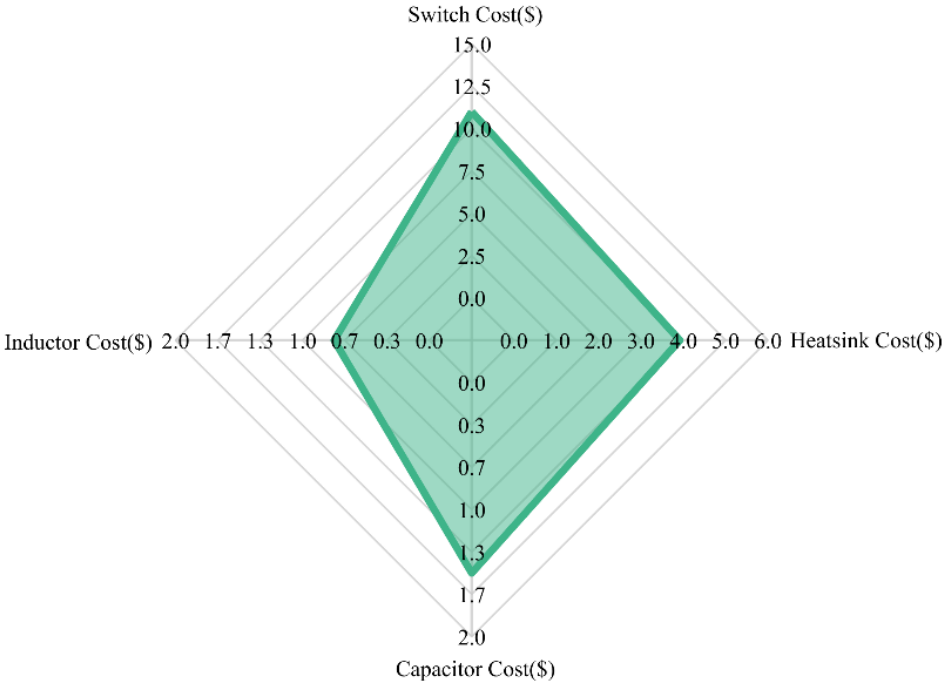

Figure 3.11 : Total cost of the efficiency constrained design.

Table 3.13 : All results comparison.

Scenario	Total Power Loss (W)	Total Volume (cm³)	Total Price (USD)
Efficiency-Constrainted	12.7	3.19	17.17
Cost-Constrainted	104.2	3.47	11.55
Volume-Constrainted	27.37	2.43	48.29

Table 3.13 presents a comparison of the optimization results under three different design scenarios: efficiency constrained, cost constrained, and volume constrained. In the efficiency constrained scenario, the system achieves the lowest total power loss at 12.7 W, with a moderate volume of 3.19 cm^3 and a total cost of 17.17 USD, reflecting a design optimized primarily for performance. The cost-constrained scenario results in the lowest total price of 11.55 USD but at the expense of significantly higher power loss (104.2 W) and slightly increased volume (3.47 cm^3), highlighting the trade off between cost and efficiency. Finally, the volume-constrained scenario yields the most compact design with a total volume of 2.43 cm^3; however, this leads to a total power loss of 27.37 W and the highest cost at 48.29 USD. These results demonstrate the impact of design priorities on the key system metrics and underscore the necessity of carefully balancing efficiency, volume, and cost according to application requirements.

4. CONCLUSIONS AND RECOMMENDATIONS

In this study, a power electronics optimization framework was developed for UAV applications, covering both the architecture of a FSBB converter and a three-phase inverter/synchronous rectifier, as well as optimization of switching frequency. The PSO algorithm was employed to select switching devices, capacitors, inductors, and heatsinks from predefined component databases while simultaneously optimizing the system's switching frequency.

The optimization process utilized a multi objective cost function considering total power loss, volume, and cost, enabling the design to be tailored toward specific objectives such as efficiency, compactness, or economic feasibility. In each scenario, the weighting factors of the fitness function were adjusted to prioritize different engineering goals, and the system was analyzed accordingly.

In the efficiency constrained scenario, the system achieved the lowest total power loss, with moderate volume and cost, reflecting a design optimized primarily for performance. In contrast, the cost constrained scenario produced the lowest overall price, albeit at the expense of significantly higher power loss and a slight increase in volume. The volume constrained scenario yielded the most compact design, but this resulted in moderate power loss and the highest cost among all cases.

Notably, the selection of certain components such as inductors, capacitors, and heatsinks remained consistent across scenarios, indicating that these elements provided balanced performance and robustness over a wide design space.

Based on these findings, it is recommended that a multi criteria optimization approach be adopted in similar power electronics design tasks. Careful adjustment of weighting factors according to application specific requirements is essential, as prioritizing efficiency, cost, or volume leads to markedly different design outcomes. Efficiency focused designs deliver superior performance but with higher cost and size; cost driven

designs minimize expenses but can compromise performance; and volume-constrained designs achieve compactness at the expense of increased cost or reduced efficiency.

Therefore, selecting an appropriate optimization strategy that aligns with the system's intended use and carefully managing trade offs between performance, cost, and size is of critical importance. In addition, future studies should aim to expand component databases and incorporate more advanced multi objective optimization techniques to explore a broader design space and further enhance design flexibility.

REFERENCES

[1] **Safran Group.** (n.d.). DC generator. https://www.safran-group.com/products-services/dc-generator

[2] **Skurka Aerospace.** (n.d.). DC brush starter generator. https://www.skurka-aero.com/product/dc-brush-starter-generator/

[3] **Liu, F., Xu, L., Li, Y., Kang, Y., & Wu, Z.** (2018). Permanent Magnet Synchronous Machine Starter/Generators based high-voltage DC parallel electric power system for the More Electric Aircraft. *The Journal of Engineering, 2018*(13).

[4] **Hao, Q., Zhang, Y., Qin, W., Wang, F., & Ding, X.** (2019). Design and implementation of hybrid UAV starter/generator module. Destech Transactions on Environment Energy and Earth Science (ICEEE).

[5] **Jiao, N., Liu, W., Meng, T., Sun, C., & Jiang, Y.** (2018). Decoupling control for aircraft brushless wound-rotor synchronous starter-generator in the starting mode. The Journal of Engineering, 2018(13), 581–586.

[6] **Xiao, D., Shi, L., Guo, Y., Han, Z., & Zhou, X**. (2018). Investigation of the working mechanism and characteristics of dual-mode doubly salient starter generator with variable winding. IET Electric Power Applications, 12(9), 1240–1246.

[7] **Zhang, Z., Liu, W., Peng, J., Zhao, D., Meng, T., Pang, J., & Sun, C.** (2017). Identification of TBAES rotating diode failure. IET Electric Power Applications, 11(2), 260–271.

[8] **Wei, Z., Liu, W., Zhang, Z., Jiao, N., Peng, J., & Meng, T.** (2018). Rotating rectifier fault detection method of wound-rotor synchronous starter-generator with three-phase exciter. *The Journal of Engineering*, 2018(13), 524–528.

[9] **Zhu, Y., Liu, W., Meng, T., Peng, J., & Jiao, N.** (2018). Rotor position estimation of wound-rotor synchronous starter/generator. The Journal of Engineering, 2018(13), 576–580.

[10] **Juan, Y., Haiyi, X., & Yang, Z.** (2021). An active control excitation method of three-stage brushless synchronous starter/generator in electric starting mode for MEA. IEEE Access, 9, 109763–109774.

[11] **Nan, C., Yao, T., & Ayyanar, R.** (2015). A 1 MHz eGaN FET based 4-switch buck-boost converter for automotive applications. 3rd Workshop on Wide Bandgap Power Devices and Applications (WiPDA).

[12] **Lordoglu, A., Gulbahce, M. O., Kocabas, D. A., & Dusmez, S.** (2021). System-level design approach for LLC converters. PCIM Europe Digital Days 2021, 1–8.

[13] **Zhang, Z., Huang, J., Jiang, Y., & Weiwei, G**. (2017). Overview and analysis of PM starter/generator for aircraft electrical power systems. CES Transactions on Electrical Machines and Systems.

[14] **General Atomics.** (n.d.). *MQ-1B Predator*. U.S. Air Force. Retrieved May 28, 2025, from https://www.af.mil/About-Us/Fact-Sheets/Display/Article/104469/mq-1b-predator/

[15] **How Stuff Works.** (n.d.). *How the Predator UAV works*. Retrieved May 28, 2025, from https://science.howstuffworks.com/predator.htm

[16] **Baykar.** (n.d.). Bayraktar TB2. Retrieved May 28, 2025, from https://baykartech.com/en/uav/bayraktar-tb2/

[17] **Jenkins, D.** (2023). *Baykar flies internally developed engine in Bayraktar TB2 UAS*. Aviation Week Network. Retrieved May 28, 2025, from https://aviationweek.com/defense/aircraft-propulsion/baykar-flies-internally-developed-engine-bayraktar-tb2-uas

[18] **Israel Aerospace Industries**. (n.d.). *IAI Heron*. Wikipedia. Retrieved May 28, 2025, from https://en.wikipedia.org/wiki/IAI_Heron

[19] **Aviation Week Network.** (n.d.). *Program Dossier: IAI Heron*. Retrieved May 28, 2025, from https://aviationweek.com/defense/program-dossier-iai-heron

[20] **Army Technology.** (n.d.). *Hunter RQ-5A / MQ-5B/C UAV, United States of America*. Retrieved May 28, 2025, from https://www.army-technology.com/projects/hunter/

[21] **Wikipedia.** (n.d.). *IAI RQ-5 Hunter*. Retrieved May 28, 2025, from https://en.wikipedia.org/wiki/IAI_RQ-5_Hunter

[22] **Turkish Aerospace Industries**. (n.d.). *Anka MALE Unmanned Aerial Vehicle*. Airforce Technology. Retrieved May 28, 2025, from https://www.airforce-technology.com/projects/anka-male-unmanned-aerial-vehicle-uav-turkey/

[23] **Bozhko, S., Yang, T., Le Peuvédic, J.-M., & Arumugam, P.** (2018). Development of aircraft electric starter-generator system based on active rectification technology. IEEE Transactions on Transportation Electrification.

[24] **Elbuluk, M. E., & Kankam, M. D.** (1997). Potential starter/generator technologies for future aerospace applications. IEEE Aerospace and Electronics Systems Magazine.

[25] **Baykar.** (n.d.). Bayraktar Akıncı. Retrieved May 28, 2025, from https://baykartech.com/en/uav/bayraktar-akinci/

[26] **General Atomics Aeronautical Systems.** (n.d.). *MQ-9A Reaper (Predator B)*. Retrieved May 28, 2025, from https://www.ga-asi.com/remotely-piloted-aircraft/mq-9a

[27] **General Atomics Aeronautical Systems.** (n.d.). *Mojave STOL*. Retrieved May 28, 2025, from https://www.ga-asi.com/remotely-piloted-aircraft/mojave

[28] **Rogoway, T.** (2023, October 17). *Smarter MQ-1C Gray Eagle Is Getting Mojave's Short Field Capabilities*. The War Zone. Retrieved May 28, 2025, from https://www.twz.com/air/smarter-mq-1c-gray-eagle-is-getting-mojaves-short-field-capabilities

[29] **Airbus.** (n.d.). *Eurodrone*. Retrieved May 28, 2025, from https://www.airbus.com/en/products-services/defence/uas/eurodrone

[30] **Military Factory.** (n.d.). *BAE Systems Mantis*. Retrieved May 28, 2025, from https://www.militaryfactory.com/aircraft/detail.php?aircraft_id=1028

[31] **Silent Falcon UAS Technologies.** (2021). *How it works*. Retrieved May 28, 2025, from https://silentfalconuas.com/how-it-works

[32] **Ubadike, O., Udekwe, D., Bonet, M. U., Momoh, M. O., Makinde, O. M., Omada, J. E., & Mohammed, A.** (2022). *Development of a BLDC motor based starter-generator for an experimental UAV*. FUW Trends in Science & Technology Journal, 7(2), 932–937. Retrieved May 28, 2025, from

[33] **Mechtex.** (n.d.). *Thermal management in BLDC motors*. Retrieved May 28, 2025, from https://mechtex.com/blog/thermal-management-in-bldc-motors

[34] **Akın, O., Bilgin, Ç., Çelik, S., & Gülbahçe, M. O.** (2022). Design of four-switch buck-boost converter with high efficiency for light electric vehicle applications. ELECO 2022 National Conference on Electrical, Electronics and Biomedical Engineering, 1–7.

[35] **Liu, Q., Qian, Q., Zheng, M., Xu, S., Sun, W., & Wang, T.** (2021). An improved quadrangle control method for four-switch buck-boost converter with reduced loss and decoupling strategy. IEEE Transactions on Power Electronics, 36(9), 10827–10841.

[36] **Mohanraj, D., Aruldavid, R., Verma, R., Sathyasekar, K., Barnawi, A. B., Chokkalingam, B., & Mihet-Popa, L.** (2022). A review of BLDC motor: State of art, advanced control techniques, and applications. *IEEE Access*, *10*, 3175011.

[37] **Copt, F., Araujo, D. M., Koechli, C., & Perriard, Y.** (2017). Dynamic winding reconfiguration of a brushless DC motor. In *2017 IEEE International Electric Machines and Drives Conference (IEMDC)* (pp. 1–6). IEEE.

[38] **Fazil, M., & Rajagopal, K. R.** (2010). A novel air-gap profile of single-phase permanent-magnet brushless DC motor for starting torque improvement and cogging torque reduction. *IEEE Transactions on Magnetics, 46*(11), 3928–3932.

[39] **NXP Semiconductors.** (2017). *Design reference manual: Sensorless field oriented control of PMSM using Kinetis Motor Suite* (Rev. 1). https://www.nxp.com/docs/en/reference-manual/DRM078.pdf

[40] **Renesas Electronics Corporation.** (n.d.). *Six-step method for brushless DC motor based on R32C/118*. https://www.renesas.com/en/document/apn/six-step-method-brushless-dc-motor-based-r32c118

[41] **Sakunthala, S., Kiranmayi, R., & Mandadi, P. N.** (2017). A study on industrial motor drives: Comparison and applications of PMSM and BLDC motor

drives. In *2017 International Conference on Energy, Communication, Data Analytics and Soft Computing (ICECDS)* (pp. 537–540). IEEE.

[42] **Kurdoğlu, A.** (2007). Brushless DC motor speed control circuit design (Master's thesis, Istanbul Technical University, Graduate School of Science and Engineering). Council of Higher Education Thesis Center. https://tez.yok.gov.tr/UlusalTezMerkezi/tezDetay.jsp?id=taecsDrBxpozXiX-q90Y0Q&no=W7K7PlgI5ASCO0lt4GbE1A

[43] **Nolan, D.** (2013). Sensorless six-step BLDC commutation (Uygulama Notu AN4220). STMicroelectronics. https://www.st.com/resource/en/application_note/dm00072008-sensorless-six-step-bldc-commutation-stmicroelectronics.pdf

[44] **Chen, C.-H., & Cheng, M.-Y.** (2006, July 9–12). A new sensorless commutation drive for brushless DC motors and alternators. IEEE International Symposium on Industrial Electronics (ISIE), Montreal, Quebec, Canada.

[45] **Caricchi, F., Crescimbini, F., Noia, G., & Pirolo, D**. (1994). Experimental study of a bidirectional dc-dc converter for the dc link voltage control and the regenerative braking in PM motor drives devoted to electrical vehicles. Proceedings of the 9th Annual Applied Power Electronics Conference and Exposition, vol. 1, 381–386.

[46] **Becerra, R. C., Ehsani, M., & Jahns, T. M.** (1992). Four-quadrant brushless ECM drive with integrated current regulation. IEEE Transactions on Industry Applications, 28(4), 833–841.

[47] **Glover, F.** (1986). Future paths for integer programming and links to artificial intelligence. Computers & Operations Research, 13(5), 533–549.

[48] **Yang, X. S.** (2010). Engineering Optimization: An Introduction with Metaheuristic Applications. John Wiley & Sons.

[49] **Talbi, E. G.** (2009). Metaheuristics: From Design to Implementation. Wiley.

[50] **Eberhart, R., & Kennedy, J.** (1995). Particle swarm optimization. Proceedings of the IEEE International Conference on Neural Networks, 4, 1942–1948.

[51] **Dorigo, M., & Stützle, T.** (2004). Ant Colony Optimization. MIT Press.

[52] **Yang, X. S.** (2009). Firefly algorithms for multimodal optimization. In Stochastic Algorithms: Foundations and Applications, 5792, 169–178.

[53] **Pandi, P. M., & Devarajan, M.** (2010). Optimization of power quality in cascaded multilevel inverter-genetic algorithm approach. In *Proceedings of the International Conference on Computer Communication and Network Technologies (ICCCNT)* (pp. 1–7).

[54] **Burkart, R.M.** (2016). Advanced modeling and multi-objective optimization of power electronic converter systems, Ph.D. Dissertation, ETH Zurich.

[55] **Coilcraft, Inc.** (n.d.). *Determining inductor power losses*. Coilcraft. Retrieved May 28, 2025, from https://www.coilcraft.com/en-us/resources/application-notes/determining-inductor-power-losses/

CURRICULUM VITAE

Name Surname **:** Emel TİMURKAYNAK SOLAK

EDUCATION **:**

- **B.Sc.** **:** 2018, Istanbul Technical University, Electrical-Electronics Faculty, Electrical Engineering

PROFESSIONAL EXPERIENCE AND REWARDS:

- 2018-Present Hardware Design Engineer - Baykar Technology

PUBLICATIONS, PRESENTATIONS AND PATENTS ON THE THESIS:

- **TİMURKAYNAK SOLAK, E.** and GÜLBAHÇE M. O., 2025, Conceptual Power Conversion Architecture for Unmanned Aerial Vehicles Utilizing BLDC Motor as Both Starter and Generator, 4. International Graduate Research Symposium-IGRS 2025